

Predictability of large-scale atmospheric motions: Lyapunov exponents and error dynamics

Stéphane Vannitsem*

*Royal Meteorological Institute of Belgium
Meteorological and Climatological Research
Avenue Circulaire, 3, 1180 Brussels
Belgium*

(Dated: March 14, 2017)

The deterministic equations describing the dynamics of the atmosphere (and of the climate system) are known to display the property of sensitivity to initial conditions. In the ergodic theory of chaos this property is usually quantified by computing the Lyapunov exponents. In this review, these quantifiers computed in a hierarchy of atmospheric models (coupled or not to an ocean) are analyzed, together with their local counterparts known as the local or finite-time Lyapunov exponents. It is shown in particular that the variability of the local Lyapunov exponents (corresponding to the dominant Lyapunov exponent) decreases when the model resolution increases. The dynamics of (finite-amplitude) initial condition errors in these models is also reviewed, and in general found to display a complicated growth far from the asymptotic estimates provided by the Lyapunov exponents. The implications of these results for operational (high resolution) atmospheric and climate modelling are also discussed.

The models describing the dynamics of the atmosphere (and of the climate system) display the property of sensitivity to initial conditions, i.e. any small error introduced in the initial conditions will grow in time until it reaches a level at which the forecast becomes useless. The atmosphere can therefore be considered as displaying a chaotic dynamics. In this review, the dynamics of the initial condition errors is explored through their usual quantifiers known as the Lyapunov exponents (valid for infinitesimally small initial errors and infinite times), together with the analysis of the dynamics of finite-size errors, in a series of atmospheric models of increasing complexity.

I. INTRODUCTION

In the early fifties, the development of digital computers opened the possibility to perform weather forecasts using equations based on the laws of hydrodynamics and thermodynamics. The first successful attempts have been obtained using a set of simplified equations based on two approximations, the hydrostatic equilibrium and the approximate geostrophic balance, which respectively postulate that the vertical pressure gradient force is equal to minus the gravitational force and the Coriolis force is approximately balanced by the horizontal pressure gradient force [1]. These assumptions reduce considerably

the number of prognostic equations and are at the origin of the well-known quasi-geostrophic system of equations [2, 3]. Since then important progresses have been made and up-to-date models based on primitive equations are used for forecasting purposes covering a large range of space scales and vertical levels [4]. These are supplemented by a considerable amount of physical parameterizations to simulate cloud, rain and ice development, radiative transfers, surface interactions, and the impact of sub-grid scale dynamics, among others.

The prospect of weather forecasting has rapidly raised the question of the limits of predictability. A lot of effort have then been devoted to answer this question whose basic properties were already identified in [5]. Thompson [5] notably shows that the imperfect knowledge of the initial conditions induces a progressive degradation of weather forecasts. In other words a small error committed on the initial conditions of the system will grow in time until it reaches the size of the distance between two randomly chosen weather situations. This property, presently known as the property of sensitivity to initial conditions (or initial states), has been subsequently discovered in the numerical integration of a low-order deterministic system by [6] – based on the convection model originally developed by Saltzman [7] and presently known as the Lorenz model – indicating the intrinsic nature of this dynamical property. This pioneering work has raised a lot of interest in the community of atmospheric and climate sciences, and a lot of researches have been devoted to the analysis of sensitivity to initial conditions in a hierarchy of atmospheric and climate models, ranging from two-dimensional barotropic models [e.g. 8–10], quasi-geostrophic models [e.g. 11–20], global circula-

* svn@meteo.be

tion models based on primitive equations [e.g. 21–23], high-resolution atmospheric (mesoscale) models [e.g. 24–26], operational weather forecasting models [e.g. 27–35] and climate models [e.g. 36–47]. See also the reviews of [4, 48–50]. These different works have explored this property and the limit of predictability at different space and timescales and they all reach the same conclusion that sensitivity to initial conditions is a generic property of models describing the atmosphere and the climate system.

It was also realized that other sources of errors are degrading the forecasts, namely errors associated with the absence of description of a set of processes, errors related to the parameterizations of subgrid-scale processes, numerical errors, boundary condition errors and external forcing errors. The three first sources are usually referred as *model error*, while the boundary condition errors and external forcing errors are considered separately. The impact of the presence of these errors on the forecasts has also been investigated in atmospheric models of various complexities [e.g. 23, 27–29, 33, 51, 52], but it is only recently that a theory has been developed [53–58], revealing the polynomial nature of the short term error dynamics, contrasting with the exponential-like behavior of initial condition errors.

In parallel to these investigations, the interest of mathematicians and theoretical physicists for the problem of sensitivity to initial conditions raised considerably and led to the development of the ergodic theory of chaos for deterministic dynamical systems [e.g. 59–61], and to the development of important quantifiers of the property of sensitivity to initial conditions, the Lyapunov exponents. One central result of this theory is that in the double limit of infinitesimally small initial errors and infinitely long times, the distance between initially close trajectories increases (or decreases) in an exponential fashion with a rate, referred as the (largest or dominant) Lyapunov exponent, which is an intrinsic property of the system’s attractor [61–65]. Deterministic systems displaying a positive Lyapunov exponent, and therefore displaying the property of sensitivity to initial conditions, are referred to as *chaotic systems*.

The chaotic nature of atmospheric flows has been investigated using tools of ergodic theory in a hierarchy of atmospheric and/or oceanic models ranging from low-order [66, 68–71], to more sophisticated, intermediate-order, models describing barotropic (2-dimensional) flows [10] and quasi-geostrophic flows [13, 15, 20, 67, 72–74]. All the results support the chaotic nature of the atmospheric models, and by extension of the atmosphere itself.

In the real world, one is usually dealing with the dynamics of finite size errors during a finite time period. The double limit appearing in the definition of the Lyapunov exponents cannot be attained and leads inevitably to consider a behavior related with the local properties of the attractor. Therefore in order to get information independent of the choice of the initial conditions, it is necessary to adopt a probabilistic approach. This aspect

has been extensively investigated in the past years and a systematic theory of error growth has been developed in the context of atmospheric sciences [58, 69, 70, 75–83] – and also in parallel in the context of turbulence [84, 85] and references therein. The key point of the approach is to incorporate information on the inhomogeneity of the dynamical properties of the solutions on the underlying attractor.

In particular, it has been shown that this practical limitation is responsible for a complex non-exponential initial behavior of the mean error for short times [70]. After this transient period, the error at all scales follows the dynamics of the dominant Lyapunov vector associated with the dominant Lyapunov exponents (provided the error is still sufficiently small), and subsequently saturates when the nonlinearities are playing a dominant role. Similar investigations have subsequently been performed in more complex convection and atmospheric models by investigating the local properties of the Lyapunov vectors associated to each exponent [15, 72, 73, 79], and the variability of their local finite-time counterparts known as the singular vectors [86–89]. This stream of ideas led to the development of what is known nowadays as *ensemble forecasts* that are operational in many weather centers around the world and which provide probabilistic information on the evolution of the atmosphere, as discussed in several reviews on ensemble forecasts [4, 48, 49].

The Lyapunov exponents (and the variability of their finite-time counterparts along the attractor of the system) are therefore key quantities for the understanding of the predictability of the atmosphere (and of climate). In the present paper, the computation of the Lyapunov exponents and of the statistical properties of the finite-time (or local) Lyapunov exponents in a hierarchy of atmospheric (and climate) models, is reviewed. Their relevance for the description of the predictability in highly detailed atmospheric and climate models is then discussed.

Section II is devoted to a general overview of the classical deterministic modelling of the atmospheric dynamics (together with a very brief introduction of the large-scale upper ocean dynamics) and Section III to the description of the computation of the Lyapunov exponents. Results obtained with a hierarchy of low-order to intermediate order atmospheric (and climate) models are presented and discussed in Section IV. The dynamics of the error is then described in Section V. Section VI is devoted to the future challenges in characterizing the predictability of atmospheric and climate flows.

II. MODELING THE ATMOSPHERIC AND OCEAN DYNAMICS

Traditional atmospheric (and climate) models are based on the classical set of conservation laws of hydrodynamics [2, 90]. For the atmosphere, these include mass balance, moisture balance, momentum balance and en-

ergy balance. These equations are complemented by a number of diagnostic relations such as the equation of state. The typical set of equations used for describing the dynamics of the atmosphere are,

the conservation of momentum,

$$\frac{d\vec{v}}{dt} = -2\vec{\Omega} \times \vec{v} - \nabla\Phi - \frac{1}{\rho}\vec{\nabla}p - \frac{1}{\rho}\vec{\nabla} \cdot \vec{\sigma} \quad (1)$$

where \vec{v} , ρ , p , $\vec{\Omega}$, Φ and $\vec{\sigma}$ are the three-dimensional velocity field, the atmospheric density, the pressure, the angular velocity of the Earth, the geopotential and the stress tensor, respectively;

the conservation of mass,

$$\frac{1}{\rho} \frac{d\rho}{dt} = -\vec{\nabla} \cdot \vec{v} \quad (2)$$

where ρ is the density of air masses;

the ideal gas law,

$$p = \rho RT \quad (3)$$

where T is the temperature and R , the gas constant;

the thermodynamic equation,

$$c_p \frac{dT}{dt} - \frac{1}{\rho} \frac{dp}{dt} = Q \quad (4)$$

where Q is the rate of heat per unit mass added to the fluid and c_p , the specific heat at constant pressure;

and the conservation equation for the water vapor content, q ,

$$\frac{dq}{dt} = E - C \quad (5)$$

where E and C are the evaporation rate and the condensation rate, respectively. This set of equations are often known as *the primitive equations* [4, 91]. They are further complemented by appropriate boundary conditions and with complicated radiative forcings and heat exchanges, all contained in the term Q , and known as *diabatic processes*. In realistic numerical weather prediction Q , E and C play a crucial role, and should be complemented by physical packages describing the formation of clouds, the development of rain, the chemical reactions, etc..., and their interaction with the dynamics described above.

These equations are usually mapped to a spherical geometry at global scale or on a regional domain of interest, and often simplified by assuming the vertical scale of the motion to be small compared with the horizontal one. The equations are further reduced to a set of ordinary differential equations through spatial discretization using finite difference schemes or truncation of the infinite expansion of the field in an appropriate functional basis, or both [2].

Starting from this set of equations, the process of forecasting consists first in identifying the phase space

point that represents most adequately the initial condition available from observation based on *data assimilation* techniques [92]. The next step is to compute numerically, by additional discretization in time, the trajectory of the dynamical system in phase space, also known as numerical model integration. To reach a high spatial resolution one includes the maximum number of degrees of freedom compatible with the computing power available. Usually the complication of the structure of operational atmospheric and climate models precludes reliable statistical analysis or a systematic exploration of the behavior in terms of the parameters.

An important class of models of the atmospheric circulation which have been used extensively for forecasting purposes, is provided by the quasi-geostrophic models [3, 93]. These models are obtained by adopting a number of assumptions in the full set of balance equations, the most important of which are: (i) the atmosphere is in hydrostatic equilibrium; (ii) the wind and pressure fields are in approximate geostrophic equilibrium so that the horizontal advection is essentially described by the non-divergent velocity field; (iii) the dynamical equations contain only the dominant contributions of a Taylor expansion of the Coriolis force.

More formally, these approximations are justified through the natural scaling of the dominant large scale flows in both the atmosphere and the ocean at mid-latitudes, for which the pressure gradient is in approximate balance with the Coriolis force. The predominance of this approximate balance is associated with a non-dimensional number known as the Rossby number, $Ro = U/(fL)$, where U and L are the typical horizontal velocity and length scales of the large scale flows and the coriolis parameter $f = 2\Omega \sin(\phi)$ where Ω is the amplitude of the angular velocity of the Earth and ϕ the latitude. For the atmosphere at midlatitudes this number is of the order of 0.1 and for the ocean of the order of 0.01, see [93] for a more detailed discussion on these scalings.

These simplifications led to an equation of conservation for the potential vorticity in pressure coordinates,

$$q = \nabla^2 \psi + f + f_0^2 \frac{\partial}{\partial p} \sigma^{-1} \frac{\partial \psi}{\partial p} \quad (6)$$

where ψ is the streamfunction, f_0 , the dominant contribution of the Coriolis force estimated at $\phi_0 = 45^\circ$, and σ , the static stability parameter,

$$\frac{\partial q}{\partial t} + (\vec{v} \cdot \vec{\nabla})q = F \quad (7)$$

where $\vec{v} = (-\partial\psi/\partial y, \partial\psi/\partial x)$ is the non-divergent horizontal velocity field and F contains all the dissipative and forcing terms. This conservation law and the notion of potential vorticity has been considerably exploited for the understanding of the large scale atmospheric dynamics, see e.g. [94]. Note that in this setting the temperature

in the atmosphere is given by

$$T_a = -\frac{f_0 p}{R} \left(\frac{\partial \psi}{\partial p} \right)_p \quad (8)$$

where R is the ideal gas constant.

Based on similar approximations, one can also deduce a conservation equation (7) for the large scale dynamics of the upper layer of an ocean (considered as homogeneous) in which the potential vorticity q is now

$$q = \nabla^2 \Psi + \beta y - \frac{1}{L_d^2} \Psi \quad (9)$$

where $\beta = df/dy$ at $\phi_0 = 45^\circ$ and $L_d = \sqrt{g'H}/f_0$ with H the depth of the water layer, and $g' = g(\rho' - \rho)/\rho$, the reduced acceleration of gravity where ρ and ρ' are the densities of two superimposed ocean layers, the lower one being an infinitely deep layer at rest [93]. Note also that an important forcing of the ocean dynamics (present in the term F in the right hand side of 7) is the wind stress at the ocean surface expressed as,

$$\frac{\text{curl}_z \vec{\tau}}{\rho H} = \frac{C}{\rho H} \nabla^2 (\psi_{lower} - \Psi_{upper}). \quad (10)$$

where the wind stress is proportional to the relative velocity between the wind in the lower atmospheric layer, \vec{v}_{lower} and the flow in the ocean upper layer, $\vec{v}_{o,upper}$, namely $\vec{\tau} = C(\vec{v}_{lower} - \vec{v}_{o,upper})$. The drag coefficient, C , characterizes the strength of the mechanical coupling between the ocean and the atmosphere and is a key bifurcation parameter in the coupled model that will be discussed later.

The dynamical systems analysis presented below consists first to embed the evolution of the system just described above in a space spanned by the ensemble of relevant variables, known as the phase space. Typical phase space variables are the values of the meteorological fields at grid points, or the coefficients of their expansions in an appropriate functional basis. Their number is usually very high (10^8 or so in operational forecasting), unless drastic truncations leading to low-order or intermediate-order models are performed. Let us now focus on the specific models that will be used in the analyses that will follow.

A. Low-order models

Low-order models have flourished in various fields of science [64], and in particular in atmospheric and climate sciences [e.g. 95–114]. These simplified models containing key ingredients of the physics of the atmosphere and/or the ocean allow for clarifying important features of the underlying dynamical properties in phase space.

For the present illustrative purpose, we will make use of a model of the atmospheric dynamics at midlatitudes developed by Charney and Straus [98], referred as the

CS model in the following, and a recent extension of this model developed for the understanding of the coupled ocean-atmosphere dynamics [115, 116]. The latter is first presented in some details and the simplifications leading to the CS model will be outlined.

The atmospheric model is based on the vorticity equation (7) defined at two superimposed atmospheric levels, say 1 and 2, which constitutes a minimal representation for the development of the so-called baroclinic instabilities at the origin of the main variability of the weather at midlatitudes [3]. The ocean dynamics confined to a single homogeneous layer is based on a vorticity equation with the potential vorticity given by (9). Finally an advection equation for the temperature in the ocean considered as a passive scalar is incorporated in the model,

$$\frac{\partial T_o}{\partial t} + (\vec{v}_o \cdot \vec{\nabla}) T_o = -\lambda(T_o - T_a) + E_R(t) \quad (11)$$

where \vec{v}_o is the (non-divergent) ocean velocity, $E_R(t)$ the radiative input in the ocean and $-\lambda(T_o - T_a)$ the heat exchange between the ocean and the atmosphere. For more details on the equations of the model and the parameters, see [115, 116].

The model is forced by short-wave radiations coming from the Sun and an energy balance scheme is redistributing the energy through long-wave radiation emissions and heat transfer between the two components of the system. The energy entering into the ocean is

$$E_R(t) = -\sigma_B T_o^4 + \epsilon_a \sigma_B T_a^4 + R_o(t). \quad (12)$$

where ϵ_a is the emissivity of the atmosphere, σ_B , the Stefan-Boltzman constant and $R_o(t)$ the net radiative input entering the ocean coming from the Sun. While for the atmosphere the radiative input is,

$$E_{a,R}(t) = \epsilon_a \sigma_B T_o^4 - 2\epsilon_a \sigma_B T_a^4 + R_a(t). \quad (13)$$

where $R_a(t)$ is fixed to $R_o(t)/3$. It is assumed that the temperature fields can be linearized around a reference temperature in both the atmosphere and the ocean as

$$T_a = T_{a,0} + \delta T_a, \quad (14a)$$

$$T_o = T_{o,0} + \delta T_o, \quad (14b)$$

where $T_{a,0}$ and $T_{o,0}$ are spatially uniform temperatures. It is also assumed that the atmosphere is dry and is not affected by effects associated with the development of rain, ice and clouds.

Also let

$$R_a(t) = R_{a,0}(t) + \delta R_a(t), \quad (15a)$$

$$R_o(t) = R_{o,0}(t) + \delta R_o(t), \quad (15b)$$

with $R_{o,0}(t)$ and $R_{a,0}(t)$ are time dependent spatially uniform shortwave radiative forcings, and $\delta R_a(t)$ and $\delta R_o(t)$, the spatially varying counterparts.

In order to mimick as close as possible the radiative input coming from the sun at midlatitudes, $R_o(t)$, used in the low-order model, is approximated as

$$R_o = R_{o,0} + \delta R_o = S_o(1 + \alpha \sin(\omega(t - \zeta))) + \kappa S_o \cos(y')(1 - 2\alpha \sin(\omega(t - \zeta))) \quad (16)$$

where $\omega = 2\pi/365 \text{ days}^{-1}$, $\zeta = 80 \text{ days}$, and y' is the latitude in non-dimensional units varying from $[0, \pi]$. κ is a free parameter varying between $]0, 1]$ and α is fixed such that the radiative input is never negative in the whole domain, $\alpha = \min(((1/\kappa) - 1)/((1/\kappa) + 2), 0.5)$. This choice also implies that the energy input in the non-autonomous case is reaching 0 at $y = \pi$ at $t \approx 355 \text{ days}$ (Winter solstice). Two free parameters are present in this relation: S_o , the energy input, and κ , the latitudinal contribution. Figure 1 displays R_o for different values of κ , the smaller the value of κ , the larger the seasonal variations. For $\kappa=0.3$, the seasonal variation is very similar to the actual evolution as discussed in [115].

A second important parameter largely influenced by the seasonal variations of the radiative input is the depth of the upper ocean layer, known as the mixed layer, interacting directly with the atmosphere as discussed in [115]. In this context we choose the following relation for the ocean depth,

$$H(t) = D_{ref} \ln \left(1 + \left(\frac{500}{R_{o,0}(t)} \right)^3 \right) \quad (17)$$

where D_{ref} is fixed to 100 m in most of the integrations performed below, unless it is explicitly stated.

The atmospheric and oceanic fields are expanded in Fourier series over the domain, $(0 \leq x' \leq 2\pi/n, 0 \leq y' \leq \pi)$, where n is the aspect ratio between the meridional and the zonal extents of the domain, $n = 2L_y/L_x$, and $x' = x/L$ and $y' = y/L$.

One retains the following set of modes for the dynamics within the ocean,

$$\begin{aligned} \phi_1 &= 2\sin(nx'/2)\sin(y'), \\ \phi_2 &= 2\sin(nx'/2)\sin(2y'), \\ \phi_3 &= 2\sin(nx')\sin(y'), \\ \phi_4 &= 2\sin(nx')\sin(2y'), \\ \phi_5 &= 2\sin(nx'/2)\sin(3y'), \\ \phi_6 &= 2\sin(nx'/2)\sin(4y'), \\ \phi_7 &= 2\sin(nx')\sin(3y'), \\ \phi_8 &= 2\sin(nx')\sin(4y'). \end{aligned} \quad (18)$$

For temperature, the same set is used, except the modes ϕ_1 and ϕ_5 for which the spatial average is different from 0. This allows to interpret the reference temperature within the ocean as a spatial temperature average.

For the atmosphere, we keep the same set of modes as in [100],

$$\begin{aligned} F_1 &= \sqrt{2}\cos(y'), \\ F_2 &= 2\cos(nx')\sin(y'), \\ F_3 &= 2\sin(nx')\sin(y'), \\ F_4 &= \sqrt{2}\cos(2y'), \\ F_5 &= 2\cos(nx')\sin(2y'), \\ F_6 &= 2\sin(nx')\sin(2y'), \\ F_7 &= 2\cos(2nx')\sin(y'), \\ F_8 &= 2\sin(2nx')\sin(y'), \\ F_9 &= 2\cos(2nx')\sin(2y'), \\ F_{10} &= 2\sin(2nx')\sin(2y'), \end{aligned} \quad (19)$$

All equations are then projected onto these sets of modes after linearizing the temperature equations around reference spatially averaged temperatures. The projection is performed using the usual scalar product,

$$\langle f, g \rangle = \frac{n}{2\pi^2} \int_0^\pi dy' \int_0^{2\pi/n} dx' f(x', y') g(x', y') \quad (20)$$

for the non-dimensional equations. It leads to 8 ordinary differential equations (ODEs) for the dynamics within the ocean, one equation for the spatially averaged ocean temperature and 6 equations for the anomaly temperature field within the ocean. In addition 20 ODEs are obtained for the atmosphere, 10 for the barotropic streamfunction field $(\psi_1 + \psi_2)/2$ and 10 for the baroclinic streamfunction field $\theta = (\psi_1 - \psi_2)/2$ (also often referred to temperature due to its direct link with Eq. (8) in this setting). An additional equation for the spatially averaged atmospheric temperature is also deduced. It forms a set of 36 ODEs which is fully described in the Supplement of [115].

The CS model [98] is a simplified atmospheric version of the model just described above without ocean, for which the radiative input is directly introduced as a forcing of the baroclinic streamfunction equation in the form of a Newtonian relaxation toward an equilibrium baroclinic streamfunction field, θ^* . The equilibrium solution, θ^* , is chosen as

$$\theta^* = \theta_1^* F_1 \quad (21)$$

in adimensional units and constant in time. This model version is supposed to mimick the dominant dynamics of the atmosphere over a land surface with an idealized orography, which is given as

$$h = h_2 F_2 \quad (22)$$

also in non-dimensional units. The development of the fields in Fourier modes is limited to the first 6 modes of 19, leading to 12 ODEs. A full description of the model is given in [98].

The model equations are integrated in time using a second order Heun method.

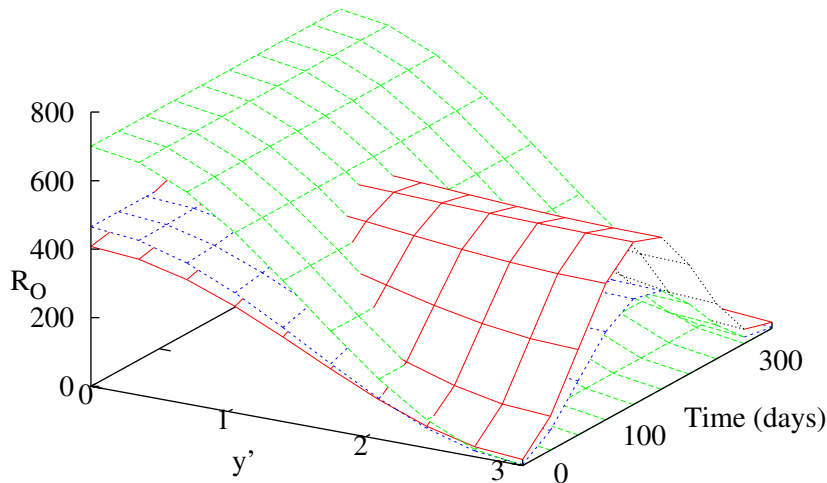


FIG. 1. Analytical expression (16) of the radiative input as a function of latitude and time for different values of κ , $\kappa = 1$ (green), $\kappa = 0.5$ (blue), and $\kappa = 0.3$, (red), with $S_o = 310 \text{ W m}^{-2}$. The latitude is displayed in adimensional units on the domain $[0, \pi]$. The unit along the vertical axis is W m^{-2} .

B. Intermediate order models

Intermediate order models have been developed in order to alleviate the limitations of high-resolution climate models whose computer time demand is very high, but still providing a realistic dynamics of the processes of interest. These are typically truncated model versions with an horizontal resolution of a few hundred of kilometers for the atmosphere.

Such a global model based on equation (7) (and denoted as QG21L3 in the following) involving three levels along the vertical has been proposed in [117]. Thanks to the relative manageability of this model (1449 variables), an extensive analysis can be performed.

The model describes the evolution of the potential vorticity (7) at three vertical levels, 200hPa, 500 hPa and 800 hPa [117]. The horizontal fields Z are expanded in series of spherical harmonics $Y_{m,n}$ truncated triangularly at wavenumber 21:

$$Z(\lambda, \phi, t) = \sum_{n=0}^{21} \sum_{m=-n}^n Z_{m,n}(t) Y_{m,n}(\lambda, \phi) \quad (23)$$

where λ , ϕ , m and n are the longitude, the latitude, the zonal and total wavenumbers, respectively. The index n represents a total (two-dimensional) wavenumber on the sphere and characterizes the size of the two-dimensional horizontal structures. The prognostic equation at each level, i , can then be written in terms of the streamfunc-

tion ψ and the potential vorticity q as

$$\frac{\partial q_i}{\partial t} = -J(\psi_i, q_i) - D(\psi_i) + S_i \quad (24)$$

where $J(\psi, q)$ is the nonlinear jacobian operator, $\partial\psi/\partial x \partial q/\partial y - \partial q/\partial x \partial\psi/\partial y$. The linear term D accounts for the effects of Newtonian relaxation of temperature, a scale selective horizontal diffusion of vorticity and temperature and a drag on the wind at the lower level whose coefficient depends on the properties of the underlying surface. Finally the time-independent spatially varying source term, S_i , constrains the solution of the model to an averaged, statistically stable, observed winter climatology ("perpetual winter" conditions). Note that all the fields are computed in non-dimensionalized units: the length unit is the earth radius (6371 km) and the time unit is half the inverse of the angular velocity of the earth ($7.29210^{-5} \text{ s}^{-1}$). The model equations are integrated in time using a leapfrog scheme (together with a Robert-Asselin filter) with a time step of 1 hour starting from a realistic potential vorticity field. The model is fully described in Appendix A of [117].

III. THE LYAPUNOV EXPONENTS

The instantaneous fields of these models are represented by points in phase space and as time elapses the phase space trajectories followed by the system's solutions tend to an invariant manifold, to which one refers

as the attractor. This reflects the dissipative character of meteorological and climate phenomena. As we are interested in characterizing the instability of the flows generated by these models, let us focus on the dynamics of (infinitely) small amplitude errors and the computation of the Lyapunov exponents.

The evolution laws of a dynamical system like the ones presented in Section II can be written in the synthetic form

$$\frac{d\vec{x}}{dt} = \vec{f}(\vec{x}, \lambda) \quad (25)$$

where \vec{x} is a vector containing the entire set of relevant variables $\vec{x} = (x_1, \dots, x_n)$ such as temperature, wind velocity, ..., projected on the relevant set of modes (or grid points) as discussed in Section II. The functions \vec{f} represent the effect of dynamical processes responsible for the change of \vec{x} , and λ denotes a set of parameters such as emission or absorption coefficients, turbulent viscosity, etc.

As mentioned in the Introduction, the initial state is never known exactly since the process of measurement and data assimilation is always subjected to finite precision. To clarify the implications of the presence of such an error we consider an initial state displaced slightly from $\vec{x}(t_0) = \vec{x}_0$ by an initial error $\delta\vec{x}_0$. This perturbed initial state generates a new trajectory in phase space and we define the instantaneous error vector as the vector joining the points of the reference trajectory and the perturbed one at a given time, $\delta\vec{x}(t)$. Provided that this perturbation is sufficiently small, its dynamics can be described by the linearized equation,

$$\frac{d\delta\vec{x}}{dt} = \frac{\partial \vec{f}}{\partial \vec{x}|_{\vec{x}(t)}} \delta\vec{x} \quad (26)$$

and a formal solution can be written as,

$$\delta\vec{x}(t) = \mathbf{M}(t, \vec{x}(t_0)) \delta\vec{x}(t_0) \quad (27)$$

where the matrix \mathbf{M} , referred as the resolvent matrix, plays an important role in error growth dynamics as revealed when writing the Euclidean norm of the error,

$$\begin{aligned} E_t &= |\delta\vec{x}(t)|^2 = \delta\vec{x}(t)^T \delta\vec{x}(t) \\ &= \delta\vec{x}(t_0)^T \mathbf{M}(t, \vec{x}(t_0))^T \mathbf{M}(t, \vec{x}(t_0)) \delta\vec{x}(t_0) \end{aligned} \quad (28)$$

One immediately realizes that the growth of E_t is conditioned by the eigenvalues of the matrix $\mathbf{M}^T \mathbf{M}$, where $(\cdot)^T$ indicates transposition (and complex conjugation in complex space if necessary).

In ergodic theory of chaotic systems, the double limit of infinitely small initial errors and infinitely long times, is usually considered [e.g. 60]. In this limit the divergence of initially closed states is determined by the logarithm of the eigenvalues of the matrix $(\mathbf{M}^T \mathbf{M})^{2(t-t_0)}$ that are referred as the Lyapunov exponents. The full set of Lyapunov exponents of a system is called the Lyapunov spectrum which are usually represented in decreasing order.

In the limit of $t \rightarrow \infty$, the eigenvectors of matrix $\mathbf{M}^T \mathbf{M}$, which are local properties of the flow and depend on the initial time t_0 , are called the Forward Lyapunov vectors [118].

Notice that the eigenvalues of the matrix $\mathbf{S} = (\mathbf{M}^T \mathbf{M})^{2(t-t_0)}$ obtained for $t \rightarrow \infty$ are equivalent to the ones of the matrix $\mathbf{S}' = (\mathbf{M} \mathbf{M}^T)^{2(t-t_0)}$ when $t_0 \rightarrow -\infty$. On the contrary, the eigenvectors of these two matrices \mathbf{S} and \mathbf{S}' – denoted as \vec{l}_i^+ and \vec{l}_i^- , respectively – are not equivalent due to the asymmetric character of the resolvent \mathbf{M} . The eigenvectors of \mathbf{S}' are called the Backward Lyapunov vectors.

Several techniques have been developed to numerically evaluate these Lyapunov exponents [119]. One of the most popular method consists in following the evolution of a set of orthonormal vectors \vec{s}_i chosen initially at random in the tangent space of the trajectory $\vec{x}(t)$. This basis is regularly orthonormalized using the standard Gram-Schmidt method to avoid the alignment of all the vectors along the unstable direction associated to the largest Lyapunov exponent. After a rapid transient, the first vector of this set, free of any constraint, will tend to the direction of maximal stretching associated to the largest Lyapunov exponent; the second vector, orthogonal to the previous one, will tend to the second most unstable direction; and so on. This set of orthonormal vectors evolving in the tangent space correspond asymptotically to the Backward Lyapunov vectors.

These vectors and their properties were extensively discussed in recent years in the literature [e.g. 15, 72, 89, 118], in particular with respect to the significance of the eigenvectors of the matrices \mathbf{S} and \mathbf{S}' . Note that these vectors are not perturbations that are covariant with the dynamics of the error in the tangent (linearized) space of the phase space trajectory. Other subspaces were then introduced, W_i

$$W_i(\vec{x}(t)) = \vec{l}_1^- \oplus \dots \oplus \vec{l}_i^- \cap \vec{l}_i^+ \oplus \dots \oplus \vec{l}_N^+ \quad (29)$$

where \oplus is the direct product [20, 59, 119, 120]. Any vector in this new subspace is covariant with the (linearized) dynamics as,

$$\mathbf{M}(\tau, \vec{x}(t')) \vec{g}_i(\vec{x}(t')) = \sigma_i(\tau, \vec{x}(t')) \vec{g}_i(\vec{x}(\tau)) \quad (30)$$

where $\sigma_i(\tau, \vec{x}(t'))$ is the amplification factor, and $\tau > t'$. Note first that the basis $\{\vec{g}_i\}$ do not form an orthogonal basis and also that in the long time limit, the amplifications give also access to the Lyapunov exponents,

$$\sigma_i = \lim_{(\tau-t') \rightarrow \infty} \frac{1}{\tau - t'} \ln (\sigma_i(\tau, \vec{x}(t'))) \quad (31)$$

The vectors $\{\vec{g}_i\}$ are called the Covariant Lyapunov vectors.

The three approaches based on the Forward, Backward or Covariant Lyapunov vectors give the same Lyapunov spectrum. However higher order properties like the variance of the local amplification rates are not equal whether

the Forward, Backward or Covariant Lyapunov vectors are used, see [120], except for the first Backward and last Forward Lyapunov vectors that have identical statistical properties as the first and last Covariant Lyapunov vectors, respectively.

Since we will focus in the present review on the Lyapunov spectra and the properties of the dominant Lyapunov exponent and vector, we will not discuss further the properties of the Covariant vectors and will leave the interested reader to explore the recent literature on that subject [20, 119–123]. We will however illustrate what is the variability (inhomogeneity) of the instability properties on the attractors of the different models by investigating the amplification rates, $\alpha_1(\tau, t) = 1/(\tau - t) \ln(\sigma_1(\tau, \vec{x}(t)))$, along the dominant Backward (or Covariant) Lyapunov vector in the spirit of [15, 70, 120, 124, 125].

IV. LYAPUNOV INSTABILITIES OF ATMOSPHERIC FLOWS

This section is devoted to the description of the Lyapunov properties of chaotic solutions found so far in the hierarchy of models discussed in Section II. The purpose is to illustrate the modifications of these properties when the number of variables of a model is increased and when dealing with a multi-scale system, and to highlight the open questions arising nowadays in atmospheric and climate sciences concerning the problem of predictability.

A. Lyapunov exponents of the low-order atmospheric system

Let us focus on the Lyapunov properties of the 12-variable low-order system introduced in Section II A, the atmosphere CS model.

Figure 2 displays the Lyapunov spectra as obtained after an integration of 10,000 days for parameter values $\theta_1^* = 0.20$, $h_2 = 0.1$ and for 2 different values of n . Note that the other parameters defined in the original paper of Charney and Straus [98] will not be discussed here for conciseness and are fixed to $2k = k' = h'' = 0.0114$, $\sigma_0 = 0.2$, $L = 5000/\pi$ km.

A clear picture emerges with 2 positive exponents, one 0, and 9 negatives ones for the two different aspect ratios explored, $n = 1.5$ and 1.77 , the latter being originally used in [98]. The solution is (hyper)chaotic and displays a Lyapunov spectrum typical of low-order systems such as the ones studied in the atmospheric context [13, 70], or in a more general physical context [64]. Note that the dominant Lyapunov exponent for $n = 1.77$ is of the same order as the amplitude of the dominant Lyapunov exponent found in more sophisticated atmospheric models as discussed later in Section IV B.

Interestingly, the spectrum is highly sensitive to the aspect ratio – i.e. a smaller domain size in the zonal di-

rection corresponds to a larger value of the aspect ratio – indicating that instability properties of the flow depends crucially on the typical wavelengths present in the dynamical system. This is reminiscent of the sensitivity of the classical baroclinic instabilities as a function of the dominant wavelength of the perturbation [3].

This specific dependence on n is also visible when the key parameter θ_1^* associated to the meridional variations of the radiative input in the domain is varied as illustrated in Fig. 3, with a higher instability for the parameter $n = 1.77$ corresponding to a smaller domain size in the zonal direction. Windows of periodic solutions are also visible reflecting the complicate structure of the bifurcation diagram for this model as usually found in other low-order models, [e.g. 62].

Another important aspect of the instability properties of this system is the high variability of the local Lyapunov exponents on the attractor. This is illustrated in Fig. 4 where the local amplification rate $\alpha_1(\tau, t)$ is plotted as a function of t with $\tau - t = 0.0056$ days and sampled every 28.4 days (corresponding to 250 non-dimensional time units). A very large variability of this amplification is visible covering values from $[-1, 1]$ day⁻¹. The standard deviation of this series is equal to 0.41 day⁻¹, a value twice as large as the value of the first Lyapunov exponent itself.

This variability on the attractor of the system indicates that the predictability of atmospheric flows highly depends on the specific underlying atmospheric situation. This natural variability of the weather skill is also experienced in real forecasts, see e.g. [49, 126], but to a lesser extent than in the current model. This point will be taken up further in the next section while investigating a higher resolution atmospheric model.

B. Lyapunov exponents of The QG3T21 model

Let us now turn to a more sophisticated atmospheric model described in Section II B. This model has 1449 degrees of freedom [15], and its solution is thus embedded in a phase space of fairly high dimension.

In Fig. 5 the first 700 Lyapunov exponents obtained after 3,000 days of integration of the standard version of the model (24) with $\tau_H = 2$ days, are displayed. For a value of the dissipation timescale of $\tau_H = 2$ days controlling the scale selective dissipation in the model (see Appendix A of [117]), the first 102 exponents are positive, the 103th is very close to zero and the next ones are negative (red filled circles in Fig. 5). This result shows that the QG model lives on a high-dimensional chaotic attractor displaying sensitivity to initial conditions. Furthermore, in view of the large number of close positive exponents, it suggests that the Lyapunov spectrum is practically continuous. The amplitude of the first exponent is equal to 0.23 days⁻¹ corresponding to a doubling time of small errors of the order of $\ln(2/0.23) \approx 3$ days, a realistic order of magnitude for the error doubling time

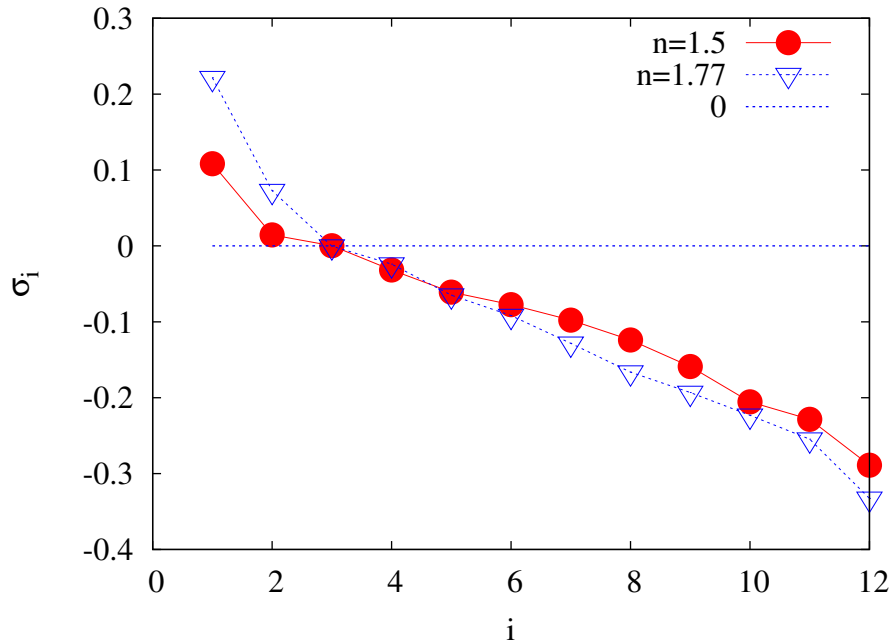


FIG. 2. Lyapunov spectra of the CS model as obtained after 10,000 days of integrations for two different aspect ratios, $n = 1.5$ (red filled circles) and $n = 1.77$ (blue triangles). The values of the Lyapunov exponents are given in day^{-1} .

in more sophisticated models at large scales [e.g. 49].

The second curve (blue triangles) in Fig. 5 displays the Lyapunov spectrum for a smaller value of $\tau_H = 1.5$ days, inducing a higher dissipation in the atmospheric model, see [15, 117]. In this case the number of positive exponents is reduced but the overall structure of the spectrum remains the same.

In order to figure out what is the sensitivity of the Lyapunov properties as a function of the forcing, S_i , a multiplicative coefficient, a , is introduced in the model equation (24) as aS_i . Figure 6 displays the variations of the amplitude of the dominant exponent and of the Lyapunov dimension as a function of a , as obtained with a set of experiments of 6,000 days of integrations. The Lyapunov dimension is defined as,

$$D_L = j^* + \frac{\sum_{j=1}^{j^*} \sigma_j}{|\sigma_{j^*+1}|},$$

where j^* is the largest j such that $\sum_j \sigma_j > 0$.

The dependence of the Lyapunov instability properties as a function of a is smooth with an increase of the Lyapunov dimension up to about 450. This smoothness contrasts with the one found in low-order models, and in particular with the CS model discussed in Section IV A, but is in agreement with the results highlighted recently in [20, 74] in other intermediate order models.

The variability of the first exponent is represented in Fig. 7a. The variability of the dominant exponent is now mainly confined to positive values except in rare occasions. This variability contrasts with the one found in the CS model for which the variability is much larger. In

order to check whether this variability is due to the specific sampling chosen, we have computed the variability of $\alpha_1(\tau, t)$ as a function of $\tau - t$ (Fig. 7b), as suggested in [80]. This variability seems already close to convergence when $\tau - t$ is of the order of 1 hour. One can therefore conclude that the variability of the dominant Lyapunov exponent is weaker in the intermediate order atmospheric model than in the low-order CS model.

These results highlight the contrast of the instability properties between low-order and intermediate order atmospheric models. In particular, a decreased variability of the local Lyapunov instabilities on the attractor of the model is observed. This feature is opening an important question to know whether this variability still decreases when the number of variables is further increased. The question is closely related to the open problem of the effective hyperbolicity (or partial hyperbolicity) of high-dimensional systems as discussed in [120, 127].

This question is not purely academic but could have important implications for operational weather forecasts since a variability of the local instability properties of high resolution models is experienced [48, 49]. Is this variability already present at the level of the large scale dynamics of atmospheric flows (as described by the quasi-geostrophic equations) or rather to processes that are not represented in this type of model, such as large scale divergent flows, convection, precipitation, gravity waves,... interfering with the large scale dynamics?

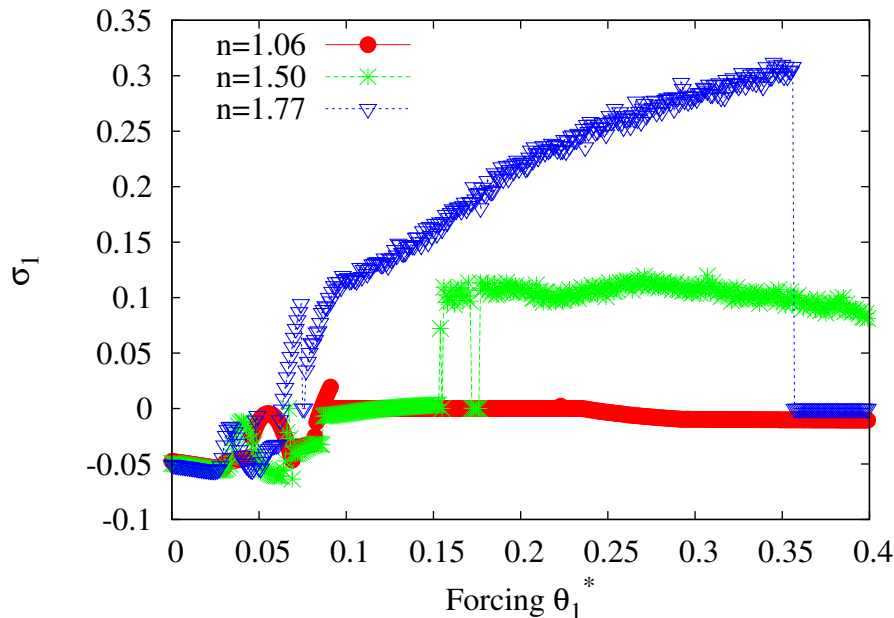


FIG. 3. First Lyapunov exponent of the CS model as a function of the thermal forcing θ_1^* for three different aspect ratios, $n = 1.06$ (red filled circles), $n = 1.5$ (green stars) and $n = 1.77$ (blue triangles). The values of the Lyapunov exponents are given in day^{-1} .

C. Lyapunov exponents of the low-order coupled ocean-atmosphere system

The atmosphere is also subject to boundary forcings coming from the other components of the climate systems that could presumably affect its predictability properties. Obvious candidates are the oceans that are interacting with the atmosphere through exchanges of momentum, mass, heat and radiations. This question is now addressed through the analysis of a low-order coupled ocean-atmosphere model described in Section II A, see also [115, 116].

The three-dimensional projections along the variables $(\psi_{a,1}, \psi_{o,2}, T_{o,2})$ of the attractors are illustrated in Fig. 8 for two different values of $C = 0.010$ and $C = 0.015 \text{ kg m}^{-2} \text{ s}^{-1}$. These attractors show fundamentally different properties, one of them displaying a dynamics around a well defined unstable periodic orbit identified in [116] (green dots). As discussed in details in [116] the development of the attractor around this unstable orbit is inducing a low-frequency variability on decadal timescales and allows for long term predictions beyond the usual 10-15 days weather forecasts. This point will be further discussed in Section V.

Figure 9 displays the Lyapunov spectra for the two attractors. A first remarkable result is the presence of a large set of Lyapunov exponents close to 0. These are associated with the presence of the ocean whose typical dissipative timescale, $1/r$, is much longer than for the atmosphere, as discussed in [120]. The Covariant Lyapunov

vectors associated with this group of exponents display angles with the tangent vector to the trajectory that are small (as compared to the other vectors), and form a near-neutral manifold of high dimension in which the error amplification (or contraction) is small. The presence of a large number of near zero exponents also implies that the Lyapunov dimension, D_L , of the system is large, even if the dimension of the unstable subspace is small. This feature may in particular have an important impact on the development of data assimilation schemes exploiting the separation of stable and unstable-neutral manifolds as proposed in [50, 128, 129].

Another important result is the small amplitude of the positive exponents when the low-frequency variability is developing in the system (green attractor of Fig. 8). In this case the system is stabler due to the strong influence of the ocean dynamics. In the climate community these two types of dynamics are usually referred to as *passive* or *active* ocean dynamics [107]. In the dynamical systems framework these qualitative changes of dynamics is explained through a bifurcation from which new types of solutions are emerging, that would not be present without the ocean-atmosphere coupling [116]. This qualitative change of dynamics has also considerable implications for the predictability of the coupled ocean-atmosphere system. This important aspect will again be addressed in Section V where the error dynamics is discussed.

Figures 10a–b display the dependence of the 1st Lyapunov exponent and the Lyapunov dimension of the coupled system as a function of the surface friction coef-

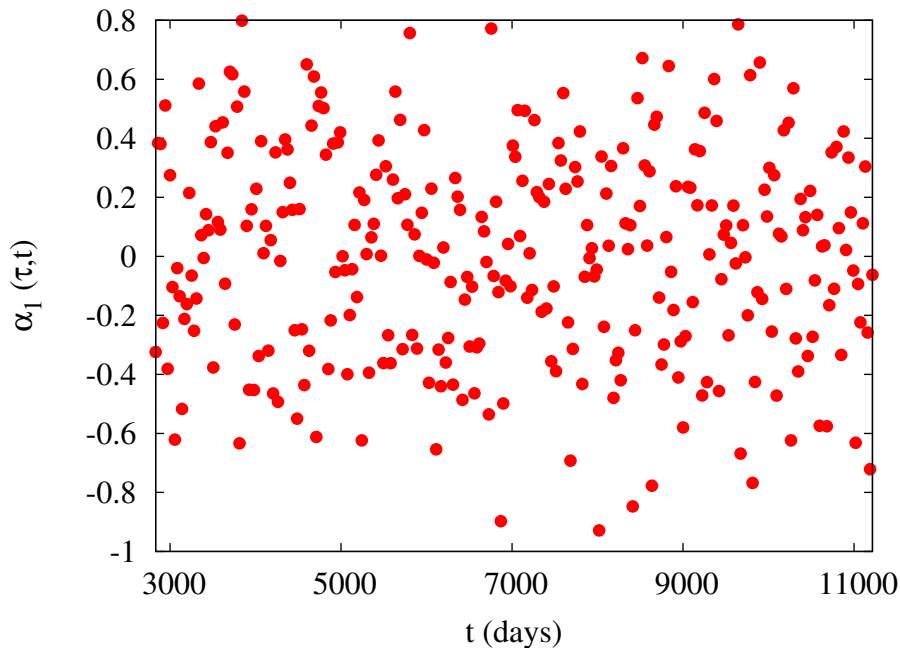


FIG. 4. Temporal variability of the local amplification rate $\alpha_1(\tau, t)$ for the CS model with $n = 1.77$, $\theta_1^* = 0.2$, and $\tau - t = 0.0056$ days. The values are sampled every 28.4 days.

ficient, C , for one specific value of $S_o = 310 \text{ W m}^{-2}$. For values of C smaller than $0.011 \text{ kg m}^{-2} \text{ s}^{-1}$, the solutions are converging toward an apparently unique attractor, e.g. the red attractor of Fig. 8. When C is further increased and for a quite substantial range of $C = [0.011, 0.014] \text{ kg m}^{-2} \text{ s}^{-1}$, the system displays solutions that can show very long transients around the attracting set present for smaller values of C , that eventually end up in a very different region of the phase space for which the attracting set displays a shape similar to the green attractor of Fig. 8. The Lyapunov spectra and dimensions were also computed for these long transient dynamics and displayed as green pluses in Figures 10a–b. Beyond that range the convergence is faster and the attracting set of the attractor of the solution resembles the green one displayed in Fig. 8.

A second result of interest is the presence of a maximum in the amplitude of the dominant exponent and of the Lyapunov dimension when the surface friction coefficient is decreased. Below a friction coefficient of about $0.0015 \text{ kg m}^{-2} \text{ s}^{-1}$ the amplitude of the dominant Lyapunov exponent decreases.

In order to understand this result, one must first realize that when C is decreased both the momentum and heat transfers between the two sub-systems are decreased [115], reducing the coupling between the two systems and the dissipation within the atmosphere. This implies that the instability properties of the flow dominated by the atmospheric dynamics is increased. When C is becoming too small a qualitative change of dynamics seems to occur but the slow convergence of the trajectories does

not allow us to clarify the specific nature of the dynamics yet. This problem is left for a future study.

Interestingly the variations of the dominant exponent and of the Lyapunov dimension in the range of interest for climate modelling, $C = [0.005, 0.020] \text{ kg m}^{-2} \text{ s}^{-1}$, look smooth, except in the transition zone $[0.10, 0.11]$. A similar picture can be drawn when changing S_o for a fixed value of C , as illustrated in Figs. 10c–d, with smooth variations of the Lyapunov instability properties as a function of the radiative forcing. This result contrasts with the usual picture that can be drawn from very low-order systems (typically of 3–4 variables) for which much more complicate bifurcation diagrams are obtained. As discussed in [74], it seems to be a natural property when the phase space dimension of the system increases.

Figure 11 illustrates the variance of $\alpha_1(\tau, t)$ as a function of $\tau - t$ for the ocean-atmosphere coupled model. A picture intermediate between the results obtained with the CS model and the QG3T21 model emerges, with a variance of $\alpha_1(\tau, t)$ converging toward a value of about 0.07 day^{-2} for $\tau - t \rightarrow 0$.

Up to now, the focus was put on the autonomous version of the low-order models but the atmosphere is strongly influenced by the natural seasonal variability. This can be taken into account in the present model by introducing realistic seasonal variations as discussed in Section II A.

Figure 12 shows the Lyapunov spectra as obtained with two different values of the friction parameter $C = 0.007$ and $C = 0.005 \text{ kg m}^{-2} \text{ s}^{-1}$, corresponding to attractors with and without low-frequency variability respectively.

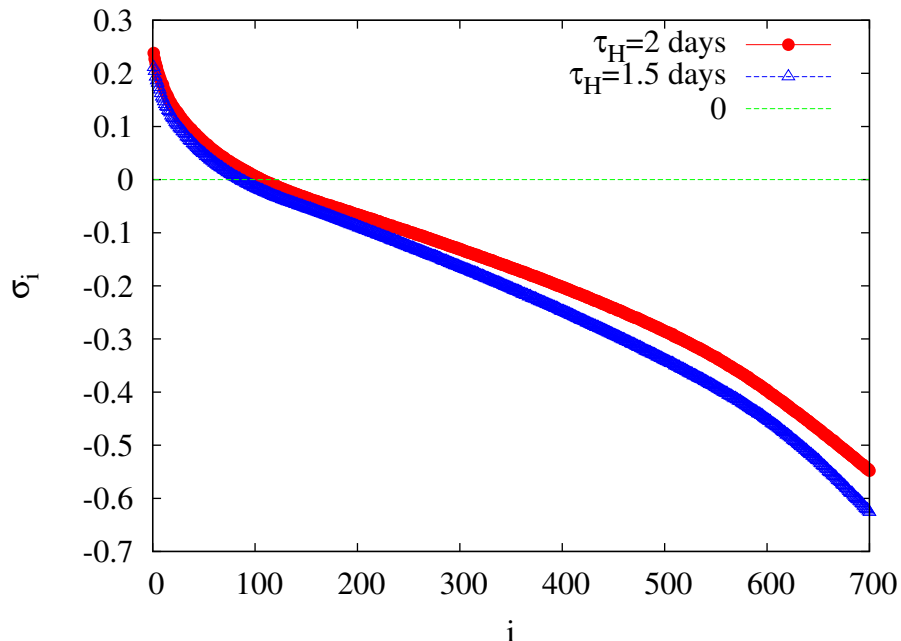


FIG. 5. Lyapunov spectra (the 700 first exponents) of the atmospheric model described in Section II B, as obtained after an integration of 3,000 days in perpetual winter conditions. Two different dissipation timescales were used, $\tau_H = 2$ days (red filled circles) and $\tau_H = 1.5$ days (blue triangles).

Both attractors are chaotic but the amplitude of the dominant Lyapunov exponent is relatively small in both cases. The main reason is the fact that when the seasonality is imposed the meridional gradient of radiative input has a smaller amplitude than in the autonomous case considered above whatever is the time of the year.

A more interesting finding is the temporal variability of the local Lyapunov exponents, $\alpha_1(\tau, t)$ with $\tau - t = 0.005$ days, sampled every 5 days. These are displayed in Fig. 13 for the two parameter values $C = 0.005$ (a) and $C = 0.007$ (c) $\text{kg m}^{-2} \text{s}^{-1}$. A zoom on a 10-year time series is also provided at panels (b) and (d) for the two parameter values. For $C = 0.007 \text{ kg m}^{-2} \text{s}^{-1}$, the local Lyapunov exponents display large modifications of their variability on a timescale of about 20,000 days with long quiescent periods as already found in the autonomous version when the low-frequency variability is setting up, contrasting with the results obtained with $C = 0.005$. When zooming in on a 10-year period (panels (b) and (d)) a seasonal signal is clearly visible with low local instabilities in summer and high in winter. This result is in agreement with the common view that the weather (large-scale flow pattern) is more predictable in summer than in winter at mid-latitudes in the Northern hemisphere.

In summary the results presented above reveals a complicate picture of the instability properties of multi-scale (autonomous and non-autonomous) systems. As the multi-scale nature of the dynamics is ubiquitous in the climate system (and in environmental modelling in gen-

eral), we suspect that such properties are generic in the real world.

V. ERROR DYNAMICS

As mentioned in the Introduction, the growth of small initial errors arising from the finite precision of the observational data and of the process of data-assimilation, is an intrinsic property of atmospheric flows. It introduces irreducible limitations in the possibility to forecast its future states beyond a predictability horizon, which may depend on the type and scale of the phenomenon under consideration. We turn now on the analysis of the error dynamics in the hierarchy of models introduced in Section II.

A. Error dynamics: generalities

As mentioned in Section III the Lyapunov exponents characterizing the predictability of chaotic systems are defined in the limit of infinitely small errors and infinitely long times. In reality, these limits are never reached and one must investigate the dynamics of finite-size initial errors on a finite-time horizon. One starts with the definition already introduced at Eq. (28) in which the classical L2 norm is used. Since one is dealing with finite-size errors, one must perform an ensemble average over the

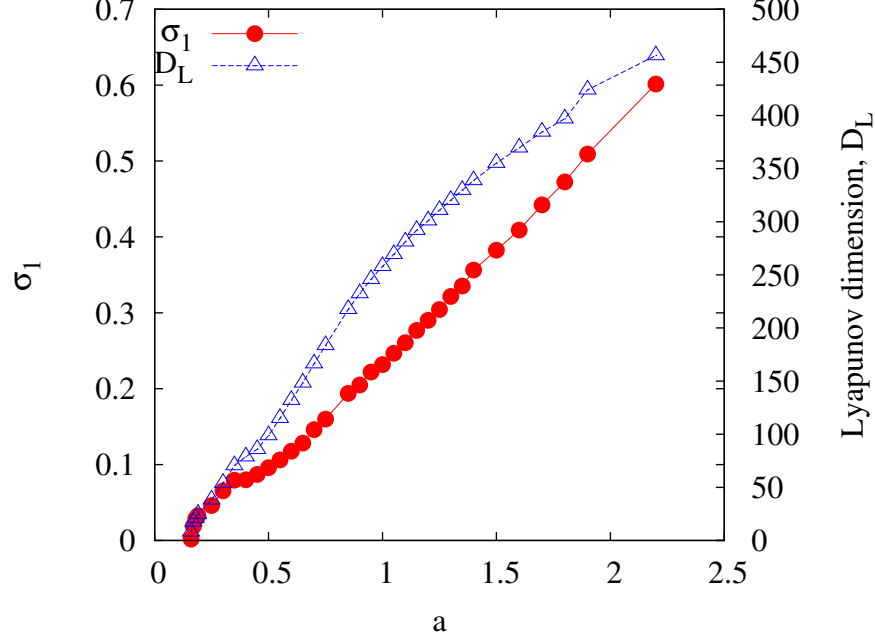


FIG. 6. Dependences of the dominant Lyapunov exponent, α_1 (red filled circles), and of the Lyapunov dimension, D_L (blue triangles), as a function of the coefficient a , multiplying the forcing, aS_i , of the atmospheric model (24).

attractor of the system,

$$\langle E_t^2 \rangle = \int d\vec{\epsilon}_0 \rho_\epsilon(\vec{\epsilon}_0) \int d\vec{x}_0 \rho_x(\vec{x}_0) (\vec{x}'(t) - \vec{x}(t))^T \mathbf{K}(\vec{x}'(t) - \vec{x}(t)) \quad (32)$$

where $\rho_\epsilon(\vec{\epsilon}_0)$ and $\rho_x(\vec{x}_0)$, are the invariant probability distribution of the initial errors and of the initial conditions on the attractor of the system (provided that the system is ergodic). A matrix \mathbf{K} is introduced in this relation allowing for choosing the specific norm of interest, for instance the energy norm or the enstrophy norm [e.g. 15]. Numerically the error evolution can be evaluated by sampling a large set of initial conditions along a reference trajectory running along the ergodic attractor of the system under consideration, and to perform additional integrations starting from slightly perturbed initial conditions.

In the following, the amplitude of the perturbations $\vec{\epsilon}$ is taken sufficiently small in order to get information on the different regimes of error growth. In this case three main regimes are expected, an exponential-like, a linear and a saturation regime, see [70, 79]. This dynamics can be empirically described by a simple logistic law of the form [28],

$$\frac{dE}{dt} = aE - bE^2 \quad (33)$$

where E is the mean amplitude of the distance, e.g. (32), between two fields, and a and b some regression

coefficients. This description is, however, a rough approximation that does not take into account the natural variability of the local amplification rates along the attractor of the system discussed in Section IV, nor the differential behavior of the error among spatial scales for which more detailed descriptions are needed, see [8, 9, 22, 27, 29, 32, 50, 70, 77].

Moreover this description is only valid provided that a short-time linearized description of the error evolution can be performed. A very enlightening analysis on the predictability of turbulent flows based on statistical arguments suggests that the propagation of small initial errors in a three-dimensional (3D) flow considerably differs from the one in a two-dimensional (2D) flow [93, 132]. Specifically, if an error is introduced at small spatial scales in the spectral domain, the error in a 3D turbulent fluid is predominantly characterized by a nonlinear local cascade propagation that will rapidly contaminate the largest scales. For 2D turbulence, the picture is different with an error dynamics involving both a local nonlinear cascade propagation and the direct amplification of errors along the large spatial scales on the same typical timescale. This implies that a linearized description of the error dynamics at large spatial scales is valid provided that the initial error is small at these large scales.

This feature can be exploited in the current analysis since the models discussed so far are based on the potential vorticity equation which provides a 2D description of the large-scale dynamics of the atmosphere. This result also justifies the use of the Lyapunov exponents for the characterization of the error dynamics in such models.

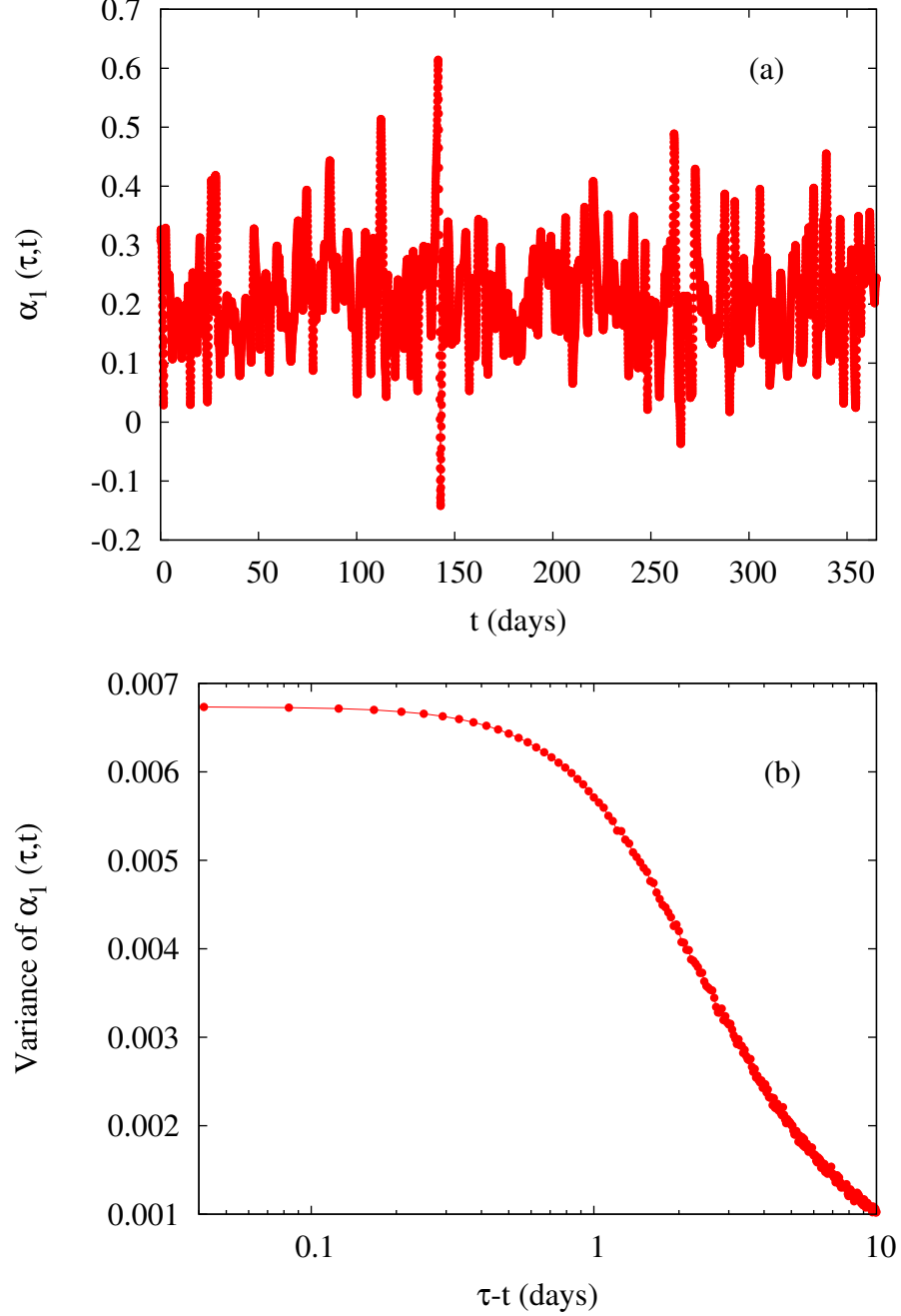


FIG. 7. (a) Temporal evolution of local amplification rate $\alpha_1(\tau, t)$ for $\tau - t = 1$ hour; (b) Variance of $\alpha_1(\tau, t)$ as a function of $\tau - t$.

B. Error dynamics in the CS model

Figure 14 displays the error evolution and the growth rate, $1/2 d/dt \ln(< E_t^2 >)$, as a function of time, as obtained with a very small initial error perturbing each variable and sampled from a gaussian distribution of mean 0 and variance 10^{-16} . The averaging is performed based on 100,000 realizations starting from different initial conditions on the attractor of the system. The key parameter

values used here are $\theta_1^* = 0.18$ and $n = 1.77$.

The overall behavior is indeed in agreement with the general description presented above with an exponential-like phase, followed by a linear regime before the final saturation. But when investigating in details the error growth rate (dotted blue curve of Fig. 14), the picture that emerges is very different with a complicate error behavior during the exponential-like regime. This complicate behavior is characterized by an initial very short er-

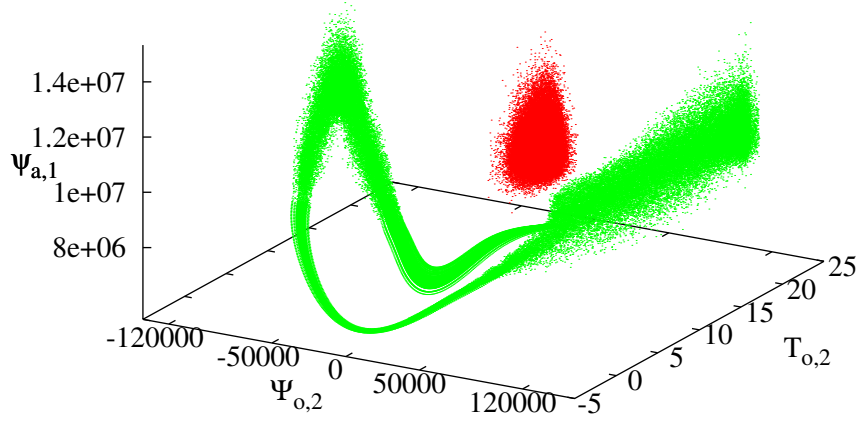


FIG. 8. Three-dimensional projection $(\psi_{a,1}, \psi_{o,2}, T_{o,2})$ of the attractors of the solutions of the low-order coupled ocean-atmosphere model described in section II A, for parameters $S_o = 310 \text{ W m}^{-2}$, $D_{ref} = 100 \text{ m}$, with two different values of $C = 0.010$ (red dots) and $C = 0.015 \text{ kg m}^{-2} \text{ s}^{-1}$ (green dots). These attractors will be referred to as the red and green attractors, respectively.

ror decrease phase for about 0.08 days (not visible on the picture), followed by important variations of the growth rate which reaches a maximum of 0.53 day^{-1} after 1.34 days. This maximum value is more than two times larger the dominant Lyapunov exponent (0.23 day^{-1}). This feature – usually referred to as superexponential – has been discussed in details in [70, 75, 120] and is mainly associated with the variability of the local Lyapunov exponents.

C. Error dynamics in the QG3T21 model

Let us now focus on the error dynamics in the QG3T21 model. Figure 15 displays the mean error evolution (red continuous curve) together with the error growth rate (blue dotted curve), as obtained from 1,000 realizations starting from different initial conditions on the attractor of the model. The initial error introduced in the model is a small amplitude error uniformly distributed in the spectral domain as in Fig. 16a.

A picture similar to the one found in the CS-model can be drawn, with an exponential-like behavior, a linear amplification of the error and a final saturation phase. The growth rate is however quite different to the one obtained with the CS-model, with a maximum not very much larger than the value of the dominant Lyapunov exponent. This difference is the result of several competing effects: (i) the variability of the local Lyapunov exponents associated with the inhomogeneity of the solution's

attractor, (ii) the quasi-continuous Lyapunov spectrum, and (iii) the choice of the initial error (and in particular of its spectral properties). The first effect is inducing a super-exponential behavior as already illustrated for the CS model. The second one is responsible for the development of a sub-exponential error dynamics as discussed in [130, 131]. The third one is modulating the initial decrease of the error and the (nonlinear) transfer of errors across scales.

In the present model, the third effect plays a dominant role as illustrated in the comparison of growth rates for different random initial errors in Fig. 15b. In this case when errors are introduced at large spatial scales (black dashed curve), the growth rate of the error is slowly increasing and reaches the value of the dominant Lyapunov exponent after about 10 days. When errors are introduced at small spatial scales (blue dotted curve), the growth rate increases rapidly and reaches a maximum after about 1.5 days which is larger than the one obtained with a uniform initial error (red continuous curve).

This dynamics is better analyzed in the spectral domain. Figure 16 shows the error evolution as a function of the total wave number n at 500 hPa. The norm used to evaluate the error is the kinetic energy norm. A first interesting feature is the decrease of the error at very large and very small spatial scales, while the error increases at intermediate scales. As stated in [15], these intermediate scales are the ones at which the dominant (Backward) Lyapunov vectors are operating, while the stable (Back-

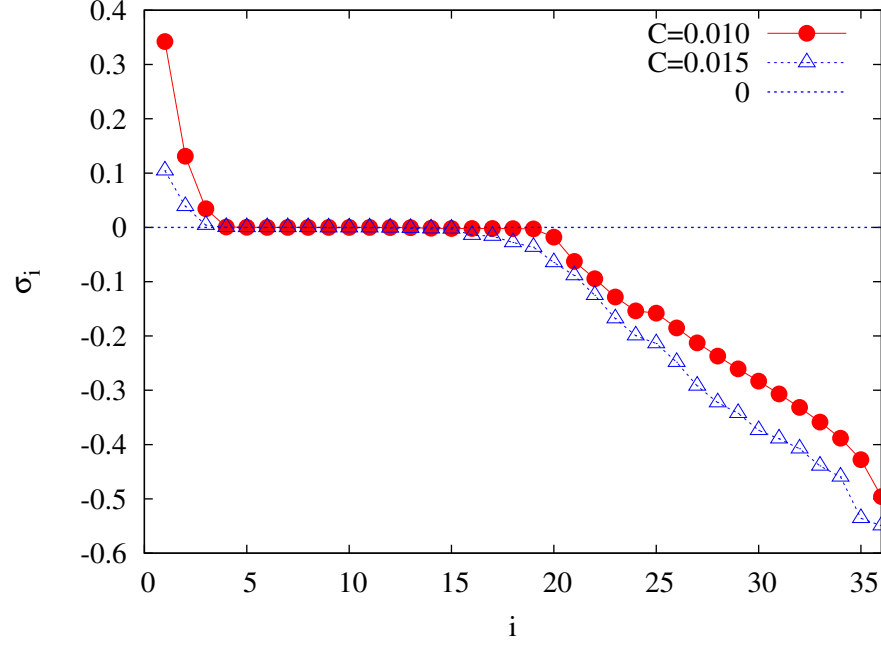


FIG. 9. Lyapunov spectra for the red (red filled circles) and green (blue triangles) attractors displayed in Fig. 8.

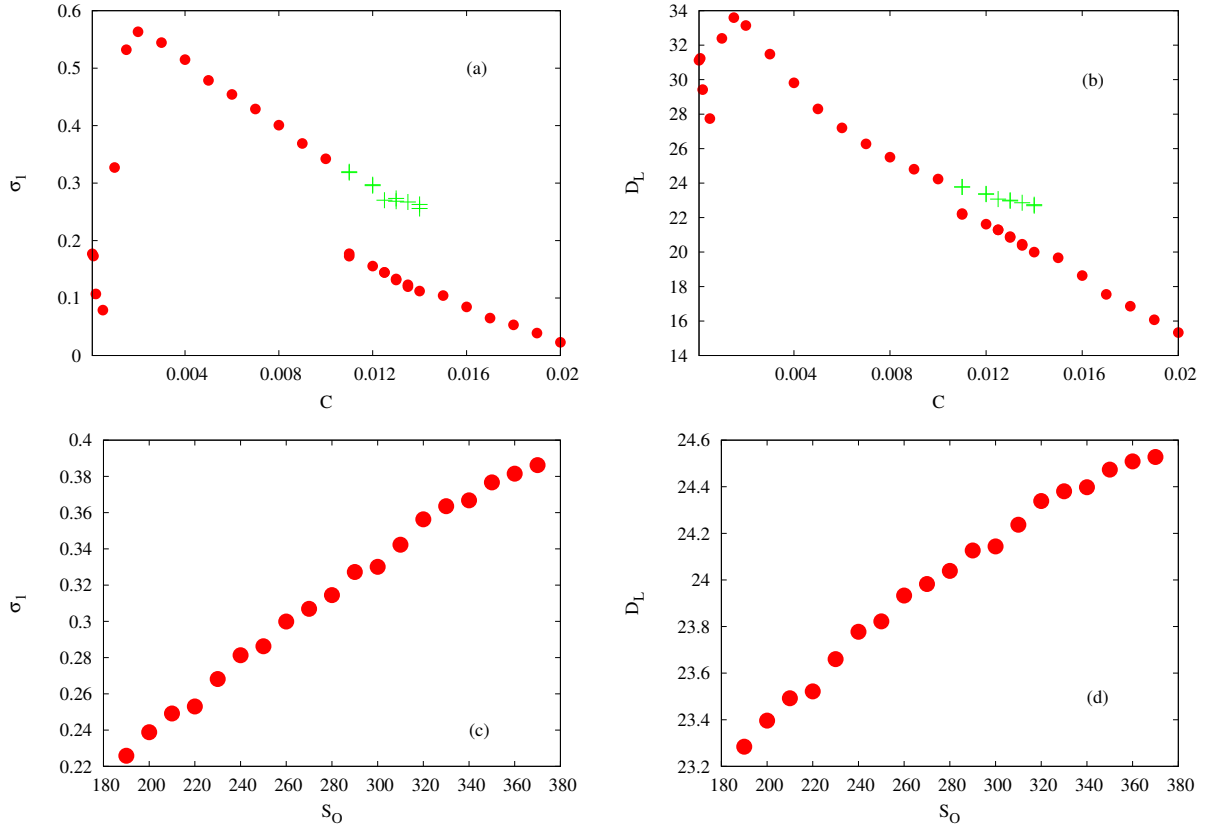


FIG. 10. First Lyapunov exponent (a) and Lyapunov dimension (b) as a function of the friction parameter C for the coupled ocean-atmosphere model with $S_o = 310 \text{ W m}^{-2}$, $D_{ref}=100 \text{ m}$ and $\kappa = 1$. The green pluses represent the results obtained with long transient trajectories that have not converged toward the final attractor yet, and living close to the red attractor of Fig. 8. (c) and (d) as (a) and (b) but as a function of S_o for $C = 0.01 \text{ kg m}^{-2} \text{ s}^{-1}$, $D_{ref}=100 \text{ m}$ and $\kappa = 1$.

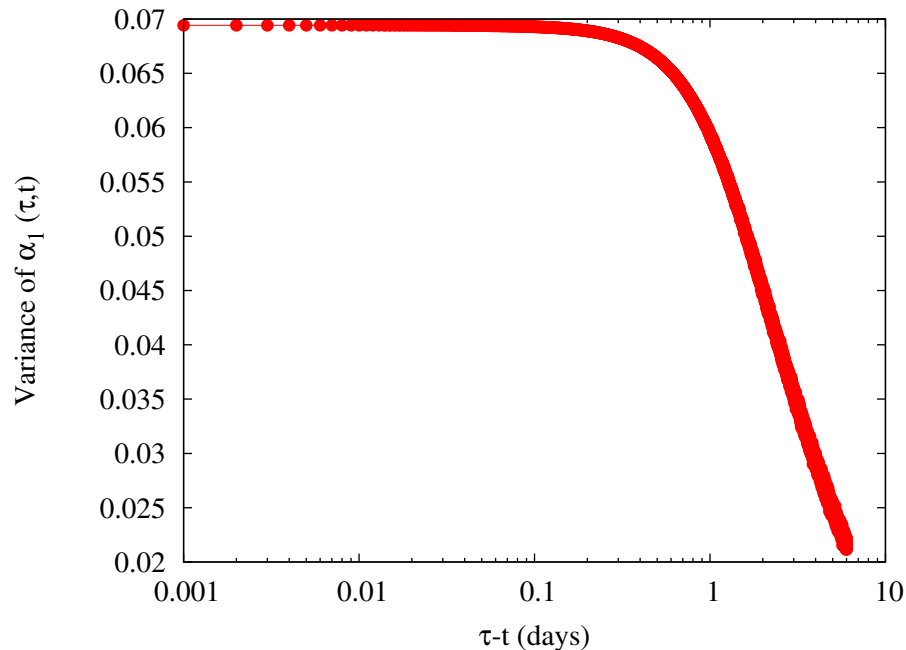


FIG. 11. Variance of $\alpha_1(\tau, t)$ as a function of $\tau - t$ for the ocean-atmosphere model, with parameters $S_o = 310 \text{ W m}^{-2}$, $D_{ref}=100 \text{ m}$, $C = 0.01 \text{ kg m}^{-2} \text{ s}^{-1}$ and $\kappa = 1$.

ward) Lyapunov vectors are mostly acting at very large and small spatial scales, inducing the specific error behavior observed in this figure.

When the initial error is confined to the very small spatial scales, a transfer (through nonlinear interactions) is occurring toward larger scales, together with the amplification along the dominant (backward) Lyapunov vectors, inducing a larger amplification rate of the error as illustrated by the blue dotted curve in Fig. 15b. When the initial error is essentially confined at large spatial scales the error evolution essentially displays an amplification according to the Lyapunov instabilities, without important transfer toward smaller scales. These behaviors are illustrated in Figs 16b-c.

The error dynamics is considerably dependent on the specific scale at which it is introduced as illustrated in Fig. 16, with a faster growth when located at small spatial scales. This feature has been exploited in the development of probabilistic forecasts in the 90th, for which strong growth were search for in order to get a sufficient variability in the multiple integrations of the ensemble forecasting systems made by the meteorological centers, e.g. [72, 86–89].

D. Error dynamics in the ocean-atmosphere model

Up to now the error dynamics has been discussed for a system – the atmosphere – displaying a variability on a range of timescales relatively close to each other, i.e. typically from a few hours up to a few days. When this sys-

tem is coupled to an ocean, highly different timescales are involved as already illustrated in the Lyapunov spectra of Section IV C. The question is therefore to know what is the nature of the error dynamics in these different subsystems and what is the impact of the ocean-atmosphere coupling on predictability. As in Section IV C we will focus on the two parameter sets explored, with and without low-frequency variability.

Figure 17a displays the mean square error evolution for the different fields present in the coupled A-O model, namely the atmospheric barotropic streamfunction (blue line referred as "Atmos stream"), the atmospheric temperature (magenta line with open squares referred as "Atmos temp"), the ocean streamfunction (green curve with crosses referred as "Ocean stream"), and the ocean temperature (red curve with pluses referred as "Ocean temp"). These curves are obtained with the parameter values corresponding to the red attractor of Fig. 8. The error rapidly amplifies for both atmospheric fields and saturates at a constant value after about 1 month (1/12 years). For the ocean the picture is very different with an increase of the error that persists beyond 100 years revealing a high potential of predictability.

If now one considers cases for which an attractor is developing around an unstable periodic orbit as the green attractor of Fig. 8, the picture is very different as illustrated in Figure 17b displaying the mean square error evolution of the first barotropic mode, ψ_1 , of the atmosphere. The two lower curves associated with the error dynamics when the attractors are developing around an unstable periodic orbit (typically the green attractor of

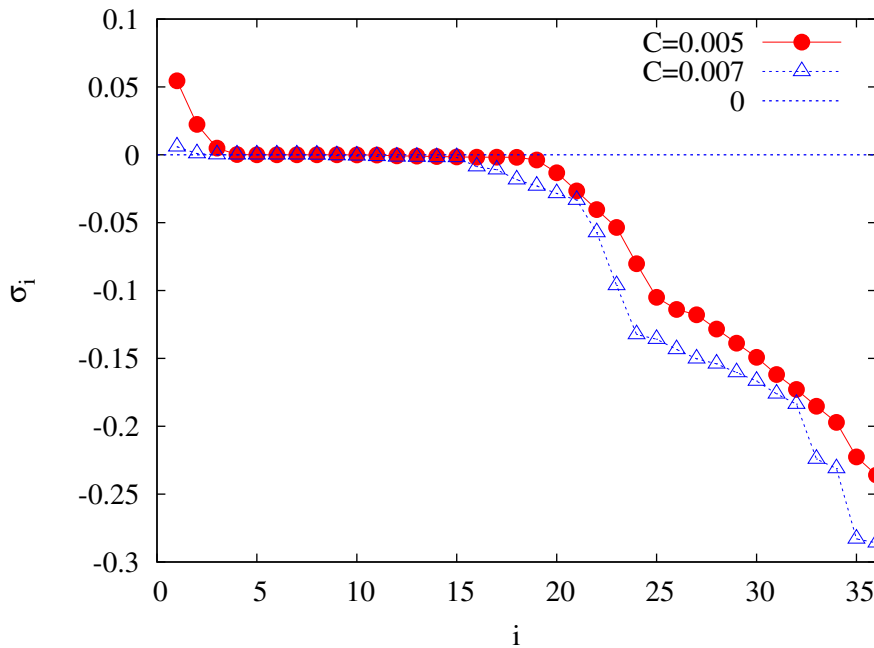


FIG. 12. Lyapunov spectra as obtained with two different values of the friction parameter $C = 0.007$ (blue triangles) and $C = 0.005$ (red filled circles) $\text{kg m}^{-2} \text{s}^{-1}$, corresponding to attractors with and without low-frequency variability, respectively. The other parameters used are $S_o = 310 \text{ W m}^{-2}$, $D_{ref}=100 \text{ m}$ and $\kappa = 0.3$.

Fig. 8) are still increasing beyond the 30 days limit detected in Fig. 17a. The behavior of the mean square error is in this case linear as a function of time suggesting a diffusive dynamics. If now we assume that the mean square error evolution can be modelled as $D(t - t_0)$ for $t > t_0 = 30$ days, the diffusion parameter, D , is larger when the reference depth of the ocean D_{ref} is larger.

This finding suggests that when the attractor is developing around the long unstable periodic orbit arising from the coupling between the ocean and the atmosphere [115, 116], some atmospheric modes can be predictable for periods much longer than the timescale of a few days (or weeks) typical of the atmospheric dynamics. This feature provides some hope in performing long term forecasts of specific observables in the atmosphere at seasonal, interannual and decadal timescales.

VI. CONCLUSIONS AND PERSPECTIVES

The Lyapunov instability properties and the error dynamics in large scale flows of the atmosphere, coupled or uncoupled to the ocean, have been explored in a hierarchy of models from low-order, $O(10)$ variables, up to intermediate order, $O(1,000)$. Two major trends are emerging when the number of variables is increased: (i) the Lyapunov spectrum can have a number of positive exponents of the order of $O(100)$ (in the standard version of the QG3T21 intermediate-order model), implying that the attractor dimension of the modelled atmosphere

is high dimensional, and (ii) the variability of the local instability properties associated with the largest Lyapunov exponent decreases.

The first trend is in line with the mathematical findings on the bounds of the attractor dimension, indicating that the atmosphere is living on a finite but high dimensional attractor [133, 134]. The second one is suggesting a smoothing of the inhomogeneity of the attractor when the number of variables is increased, and it opens important questions on the characteristics of the instability properties of the solutions in the limit of an infinite number of modes, i.e. for the continuous partial differential equations (quasi-geostrophic equations) discussed in Section II.

From a practical point of view, it is well known that the predictability of large-scale weather patterns is highly dependent on the specific initial weather situation selected [48, 49]. This suggests that this inhomogeneity is also present in high resolution atmospheric models but to which extent it resembles the one described in the quasi-geostrophic model or not, is still open. A possible way to address this question is to extend the Lyapunov analysis to high-dimensional quasi-geostrophic models of the order of $O(10,000, 100,000)$ variables.

Yet, even if this analysis would provide interesting information on the smoothness of the attractor's instability properties, it is not the end of the story. When the resolution of such models is increased, their validity in describing the dynamics of the atmosphere (and the ocean) is questionable. In this case one must go back to the

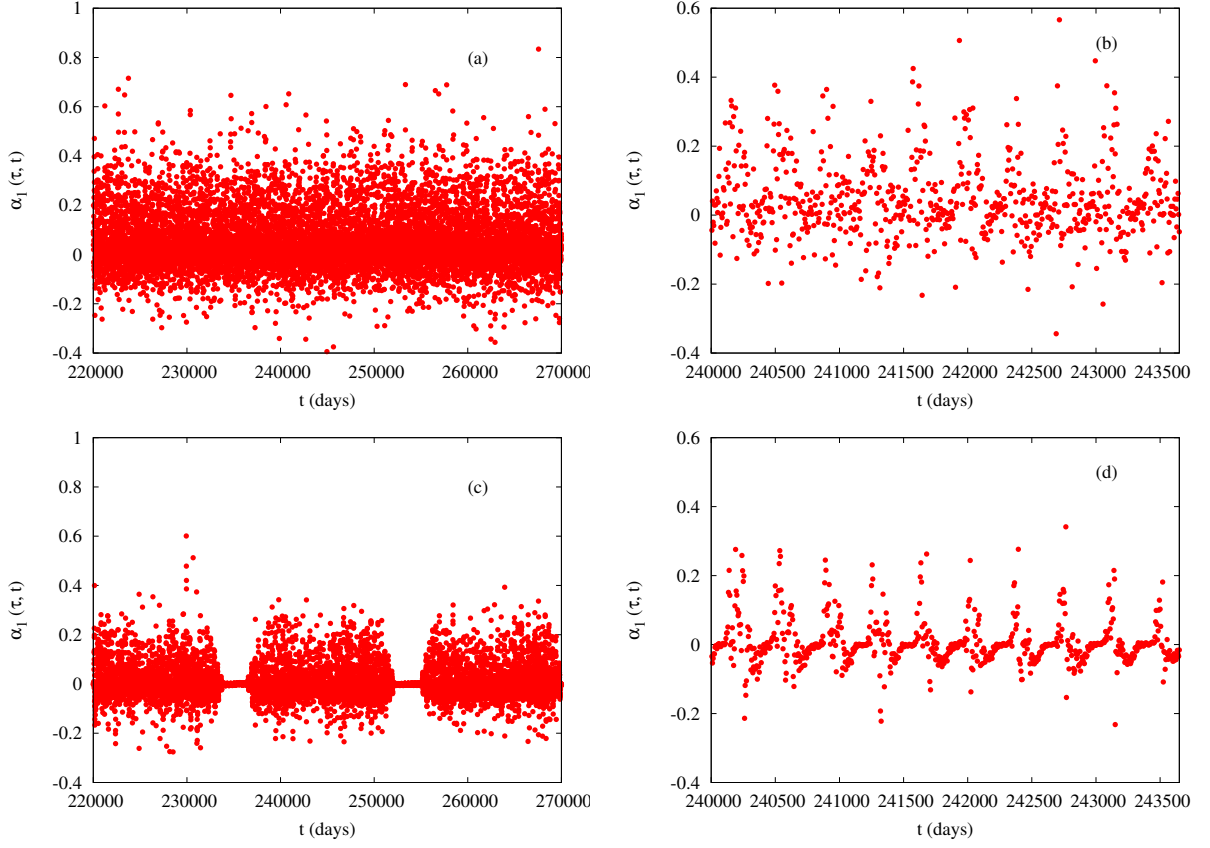


FIG. 13. Temporal variability of the local Lyapunov exponents, $\alpha_1(\tau, t)$, as obtained with $\tau - t = 0.005$ days and sampled every 5 days, for the two parameter values (a) $C = 0.005$ and (c) $C = 0.007 \text{ kg m}^{-2} \text{ s}^{-1}$. A zoom on a 10-year time series is also provided at panels (b) and (d) for the two parameter values. The other parameters used are $S_o = 310 \text{ W m}^{-2}$, $D_{ref} = 100 \text{ m}$ and $\kappa = 0.3$.

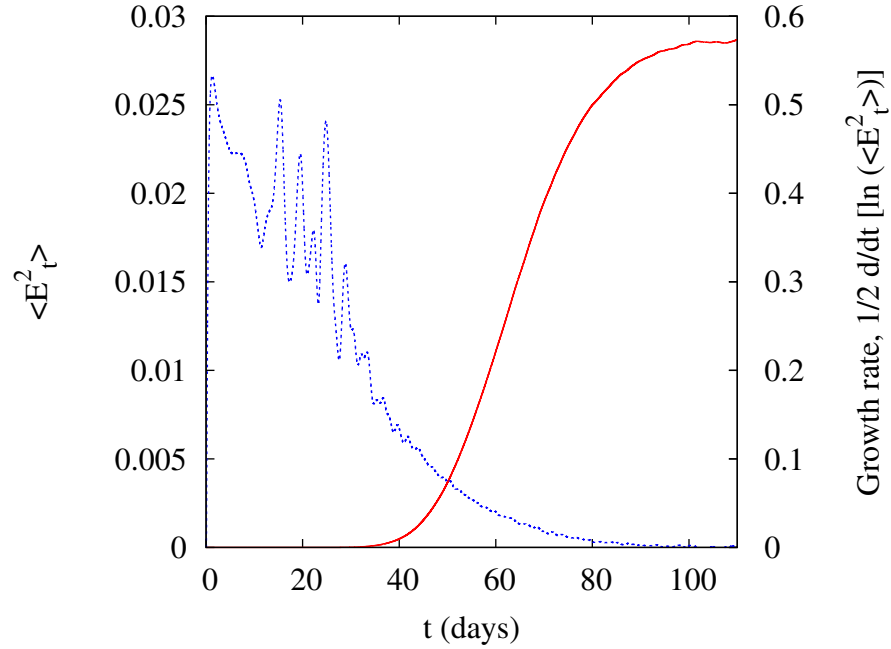


FIG. 14. Mean square error (red continuous curve) evolution and error growth rate (blue dotted curve) for the CS model, averaged over 100,000 realizations starting from initial conditions sampled on the attractor of the model.

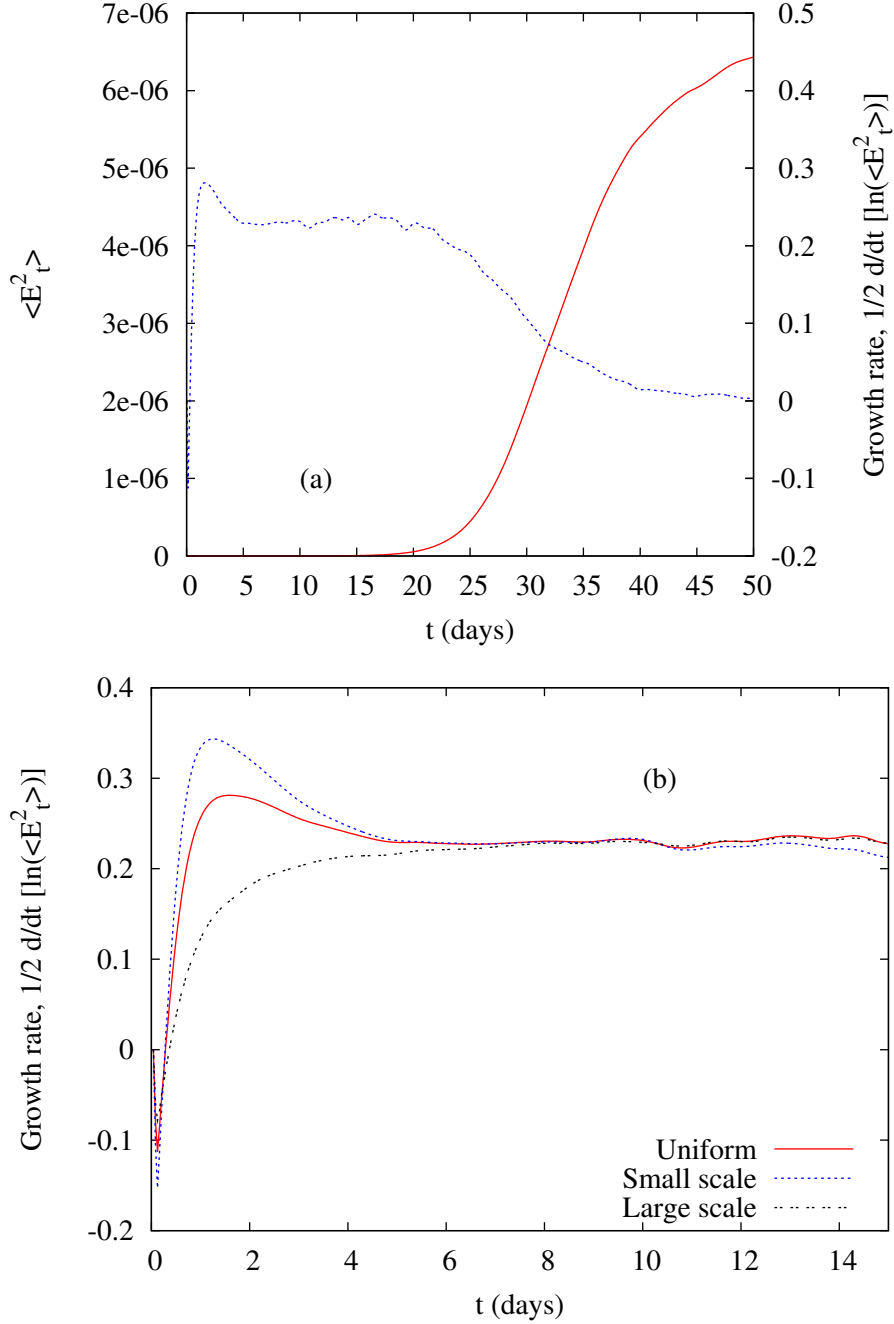


FIG. 15. (a) Mean square error evolution (red continuous curve) and growth rate (blue dotted curve) as obtained from 1,000 realizations of the error evolution starting from different initial conditions on the attractor of the QGT21L3 model. (b) Growth rate of the error, (red continuous curve) for a uniform initial error in the spectral domain (in the kinetic energy norm), (black dashed curve) for an initial error predominantly located at large spatial scales, and (blue dotted curve) for an initial error predominantly located at small spatial scales. See also Fig. 16 for the specific repartition of the error in the spectral domain.

original primitive equations discussed in the beginning of Section II, and to study the impact of the dynamics of the additional variables.

In this perspective, one particularly interesting work has been done by Ubaldi and Trevisan [26] in which they have studied the full primitive equations integrated at the

cloud-resolving scale of 2.2 km resolution, with 50 vertical levels. In this context they have studied the Bred vectors that are *finite-size* unstable structures emerging along the model trajectory. If their amplitudes is sufficiently small these are providing information on instability properties of the flow closely related to the Backward

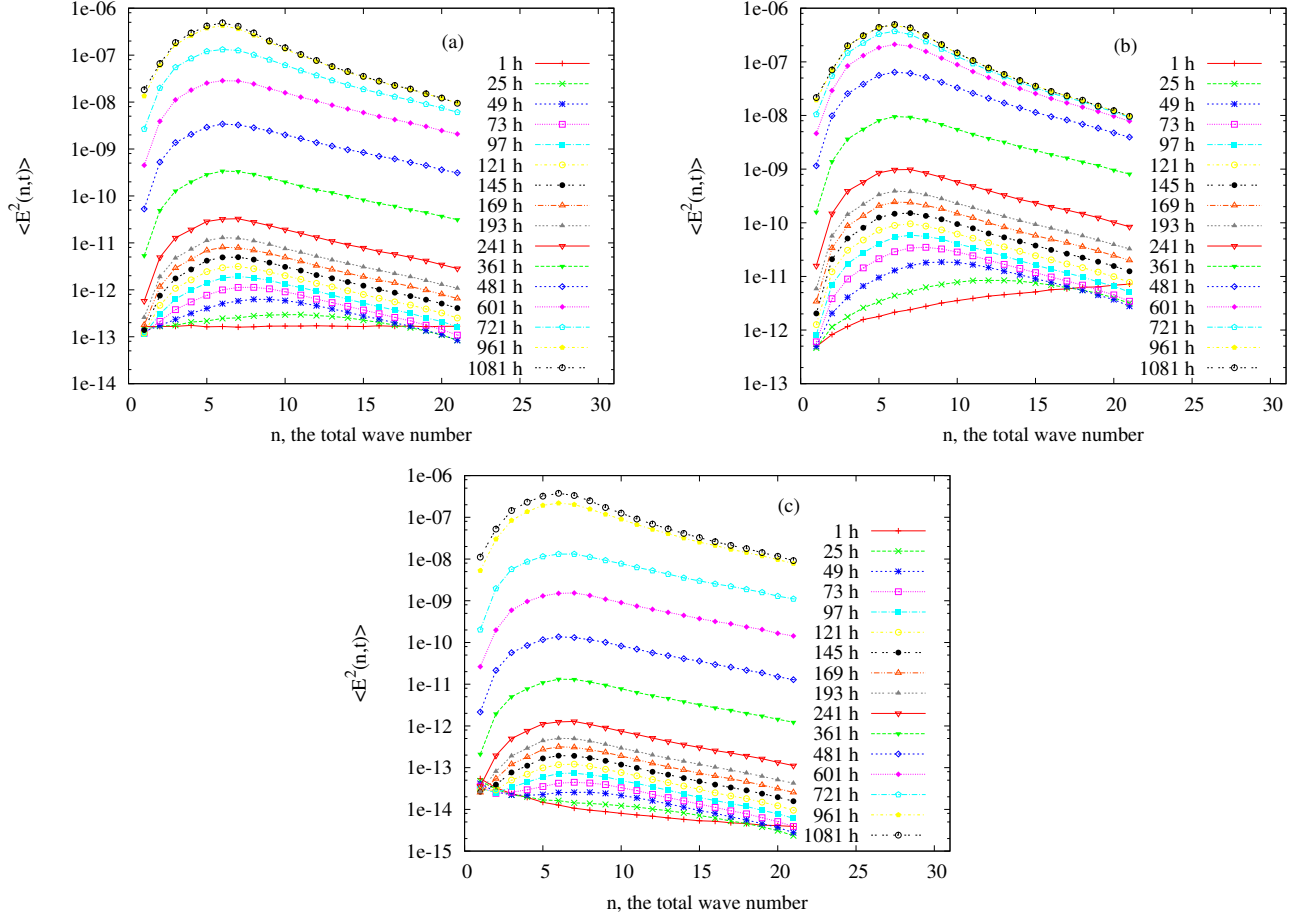


FIG. 16. (a) Mean square error evolution for the QGT21L3 model, averaged over 1,000 realizations, as a function of the total wavenumber n for different forecasting lead times from 1 hour up to 1081 hours. The initial error is uniformly distributed as a function of n in the energy norm. (b) and (c) As in (a) but for an initial error dominating the smallest and largest spatial scales, respectively.

Lyapunov vectors [72]. In the case of small-amplitude Bred vectors, they found that the dominant ones describe small convective-scale instabilities and that their number is very large. Moreover their growth rates are much larger than any perturbation acting at the large spatial scales of the flow (and much larger than the ones displayed in the present review). This result is consistent with the theoretical considerations presented by Vallis [93, 132], indicating that the dynamics of the error in a three-dimensional turbulent system – as it is the case in the high-resolution experiment of Ubaldi and Trevisan – is saturating rapidly at all the scales below 10 km, and that predictability is limited to a few hours.

These results are obviously suggesting that the development of very high resolution models at 1 km or smaller would lead to a very small gain in terms of predictability due to the rapid saturation of the error at small spatial scales, and one should therefore temper us in developing such models except if the forecast at a lead time of one or two hours is providing important information for the society. In such a case a very performant data

assimilation system would also be needed in order to reduce considerably the actual level of error. This is a very expensive process in terms of maintenance (man power), high-quality observing systems and computer power. In the sake of reducing the potential cost, it might be better to avoid such high resolution forecasts. Yet, these very high resolution forecasts should be necessary in some very specific and dangerous weather situations arising from time to time. In an operational environment a procedure should be developed in order to evaluate the necessity to perform very high resolution forecasts. This procedure could be based on storminess warnings that can be gathered from lower resolution model integrations.

Nowadays operational forecasting systems contain stochastic schemes emulating the presence of model errors. This approach allows for getting more reliable ensemble forecasts as discussed in [34, 135], but also for improving climatological aspects of the models such as correcting the mean or the variance of specific variables [e.g. 136]. This however implies that an increase of uncertainty is introduced, inducing in particular a larger

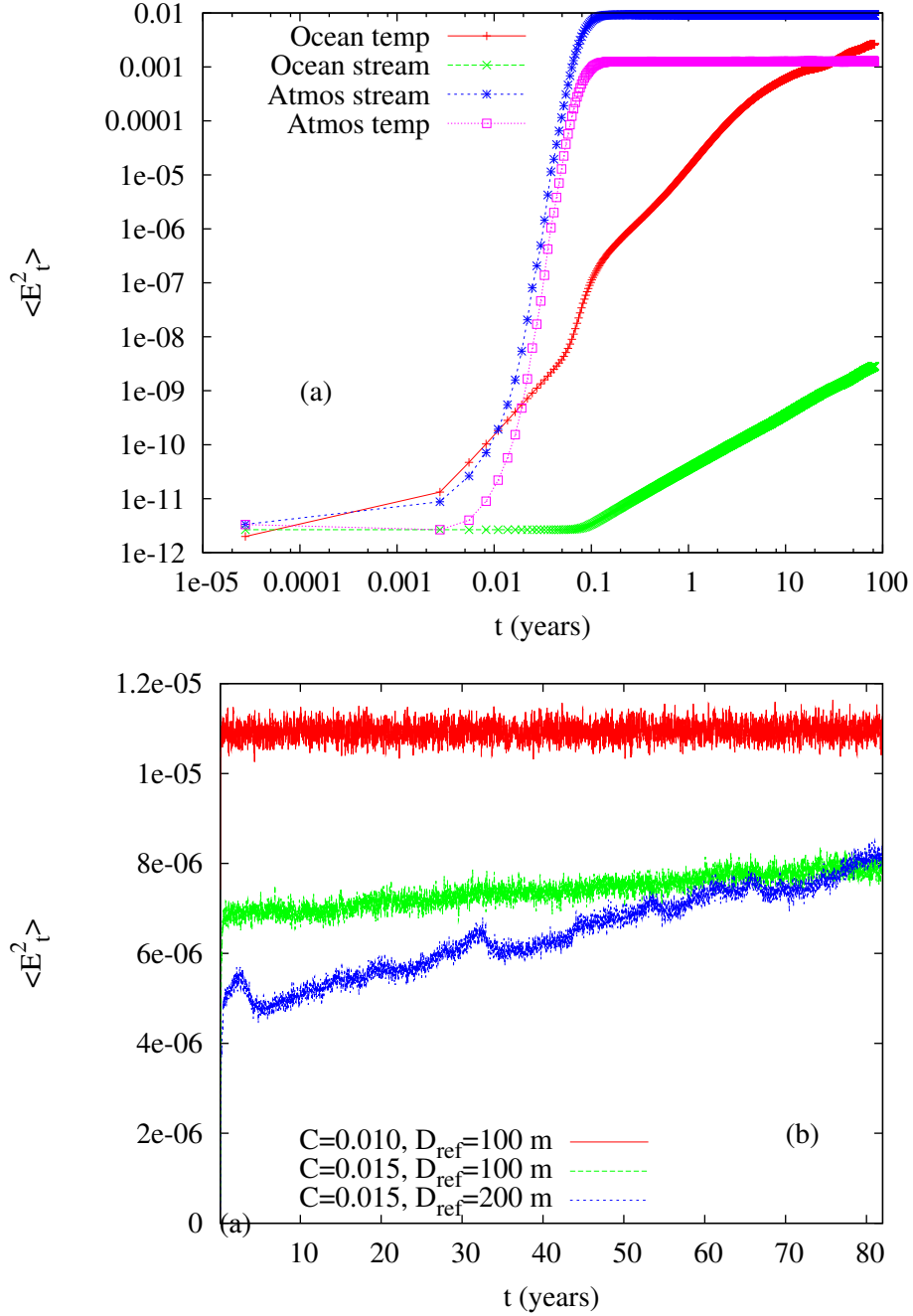


FIG. 17. (a) Mean square error evolution for the ocean-atmosphere model, for the atmospheric barotropic streamfunction (blue stars), the atmospheric temperature (magenta open squares), the ocean streamfunction (green crosses), and the ocean temperature (red pluses). The model parameter values used are $S_o = 310 \text{ W m}^{-2}$, $D_{ref} = 100 \text{ m}$, $\kappa = 1$ and with $C = 0.010 \text{ kg m}^{-2} \text{ s}^{-1}$. (b) as in (a) but for the first barotropic streamfunction mode, ψ_1 , only and for parameters: $S_o = 310 \text{ W m}^{-2}$, $D_{ref} = 100 \text{ m}$, $\kappa = 1$, $C = 0.010 \text{ kg m}^{-2} \text{ s}^{-1}$ already used in Fig. (17a) (red continuous curve), $S_o = 310 \text{ W m}^{-2}$, $D_{ref} = 100 \text{ m}$, $\kappa = 1$, $C = 0.015 \text{ kg m}^{-2} \text{ s}^{-1}$ (green dashed curve), and $S_o = 310 \text{ W m}^{-2}$, $D_{ref} = 200 \text{ m}$, $\kappa = 1$, $C = 0.015 \text{ kg m}^{-2} \text{ s}^{-1}$ (blue dotted curve).

error for short times [55, 56]. Another important issue is therefore to understand the role of stochastic forcings on the predictability of atmospheric and oceanic flows. Theoretical and practical analyses are therefore necessary in the line of the works of [137–140].

Finally the problem of forecasting atmospheric phenomena on timescales longer than the typical limit of weather forecasts, say 10 days, is a challenging problem for our society. As we demonstrate in the present review in the context of an idealized coupled ocean-

atmosphere model, long term forecasts of specific atmospheric variables are possible, provided the atmosphere is (strongly) coupled to climate components with longer typical timescales. This increase of forecast skill at seasonal and interannual timescales is already well known in the Tropical regions due to the strong coupling between the ocean and the atmosphere [e.g. 141]. Several climate forecasting models are also currently suggesting that there is some skill of the climate system at midlatitudes at seasonal and interannual timescales, although the signal is rather weak [e.g. 142]. The understanding of the origin of this long term skill and our ability to improve the long term forecasts are still fields of research in their infancy. The exploration of the coupling

between the ocean and the atmosphere (and other climate components) in the context of low and intermediate order models are important steps in that direction [115, 116, 143, 144].

ACKNOWLEDGMENTS

The comments of C. Nicolis and two anonymous reviewers on an earlier version of this manuscript were highly appreciated. This work is supported, in part, by the Belgian Science Policy Office under contract BR/121/A2/STOCHCLIM.

-
- [1] Charney, J. G., J. Meteorol., **4**, 135 (1948).
 - [2] Haltiner, G., and R.T. Williams, *Numerical prediction and dynamical meteorology*, Wiley and Sons (New York, 1980).
 - [3] Holton, J. R., *An introduction to dynamic meteorology*, Academic Press (New York, 1979).
 - [4] Kalnay, E., *Atmospheric Modeling, Data Assimilation and Predictability*, Cambridge University Press (Cambridge, 2003).
 - [5] Thompson, P. D., Tellus, **9**, 275 (1957).
 - [6] Lorenz, E. N., J. Atmos. Sci., **20**, 130 (1963).
 - [7] Saltzman, B., J. Atmos. Sci., **19**, 329 (1962).
 - [8] Lorenz, E. N., Tellus, **21**, 289 (1969).
 - [9] Basdevant, C., B. Legras and R. Sadourny, J. Atmos. Sci., **38**, 2305 (1981).
 - [10] Legras B. and M. Ghil, J. Atmos. Sci., **42**, 433 (1985).
 - [11] McWilliams, J. C. and H. S. Chow, J. Phys. Oceanogr., **11**, 921 (1981).
 - [12] Vallis, G. K., J. Atmos. Sci., **40**, 10 (1983).
 - [13] Malguzzi, P., A. Trevisan and A. Speranza, Ann. Geophys., **8**, 29 (1990).
 - [14] Barkmeijer J., P. Houtekamer and X. Wang, Tellus, **45A**, 424 (1993).
 - [15] Vannitsem, S., and C. Nicolis, J. Atmos. Sci., **54**, 347 (1997).
 - [16] Vannitsem, S., and C. Nicolis, Q. J. R. Meteorol. Soc., **125**, 2201 (1998).
 - [17] Vannitsem, S., Tellus, **53A**, 56 (2001).
 - [18] Trevisan, A., F. Pancotti, and F. Molteni, Q. J. R. Meteorol. Soc., **127**, 343 (2001).
 - [19] Morss, R.E., C. Snyder, Richard Rotunno, J. Atmos. Sci., **66**, 3115 (2009).
 - [20] Schubert, S. and V. Lucarini, Q. J. R. Meteorol. Soc., **141**, 3040 (2015).
 - [21] Tribbia, J. J. and Baumhefner, D. P., J. Atmos. Sci., **45**, 2306 (1988).
 - [22] Schubert, S.D., and M. Suarez, J. Atmos. Sci., **46**, 353 (1989).
 - [23] Tribbia, J. J., and D. P. Baumhefner, Mon. Wea. Rev., **132**, 703 (2004).
 - [24] Bei, N. and F. Zhang, Q. J. R. Meteorol. Soc., **133**, 83 (2007).
 - [25] Hohenegger C. and Ch. Schär, Bull. Amer. Meteor. Soc., **88.11**, 1783 (2007).
 - [26] Ubaldi, F. and A. Trevisan, Nonlin. Proc. Geophys., **22**, 1 (2015).
 - [27] Leith, C. E., Ann. Rev. Fluid Mech., **10**, 107 (1978).
 - [28] Lorenz, E. N., Tellus, **34**, 505 (1982).
 - [29] Dalcher, A. and E. Kalnay, Tellus, **39A**, 474 (1987).
 - [30] van den Dool, H. M. and S. Saha, Mon. Wea. Rev., **118**, 128 (1990).
 - [31] Stroe, R. and J.-F. Royer, Ann. Geophys., **11**, 296 (1993).
 - [32] Savijarvi, H., Mon. Wea. Rev., **123**, 212 (1995).
 - [33] Simmons A. J., R. Mureau and T. Petroliaigis, Q. J. R. Meteorol. Soc., **121**, 1739 (1995).
 - [34] Buizza, R., Q. J. R. Meteorol. Soc., **136**, 1020 (2010).
 - [35] Herrera, M., I. Szunyogh, J. Tribbia, Mon. Wea. Rev., **144**, 2739 (2016).
 - [36] Shukla, J., J. Atmos. Sci., **38**, 2547 (1981).
 - [37] Roads, J. O., J. Atmos. Sci., **44**, 3495 (1987).
 - [38] Palmer, T. N. and S. Tibaldi, Mon. Wea. Rev., **116**, 2453 (1988).
 - [39] Brankovic C., T. N. Palmer and L. Ferranti, J. Climate, **7**, 217 (1990).
 - [40] Goswami, B. N., S. Selvarajan, and V. Krishnamurty, Proc. Indian Acad. Sci., **102**, 49 (1993).
 - [41] Palmer, T. N., In: Decadal climate variability; dynamics and predictability. NATO ASI Series, **I 44**, Springer, 83 (1996).
 - [42] Chen Y.-Q., D. Battisti, T. N. Palmer, J. Barsugli and E. S. Sarachik, Mon. Weather. Rev., **125**, 831 (1997).
 - [43] Corti, S. and T. N. Palmer, Q. J. R. Meteorol. Soc., **123**, 2425 (1998).
 - [44] van den Dool, H. M., P. Peng, A. Johansson, M. Cheliah, A. Shabbar and S. Saha, J. Climate, **19**, 6005 (2006).
 - [45] Mu Mu, and W. Duan, J. Geophys. Res., **112**, D10113 (2007).
 - [46] Duan W., X.C. Liu and K.Y. Zhu, J. Geophys. Res., **114**, C04022 (2009).
 - [47] Delsole T., X. Yan, P. Dimeyer, M. Fennessy, E. Alshuler, J. Climate, **27**, 300 (2014).
 - [48] Ehrendorfer M., Meteorologische Zeitschrift, **6**, 147 (1997).
 - [49] Yoden, S., J. Meteorol. Soc. Japan, **85B**, 77 (2007).
 - [50] Trevisan, A., and L. Palatella, Int. J. Bifurc. and Chaos, **21**, 3389 (2011).

- [51] Vannitsem, S., J. Atmos. Sci., **63**, 1659 (2006).
- [52] Boisserie, M., P. Arbogast, L. Descamps, O. Pannekoek, L. Raynaud, Q. J. R. Meteorol. Soc., **140**, 846 (2014).
- [53] Orrell D., L.A. Smith, T. Palmer, J. Barkmeijer, Nonlin. Proc. Geophys., **8**, 357 (2001).
- [54] Vannitsem, S., and Z. Toth, J. Atmos. Sci., **59**, 2594 (2002).
- [55] Nicolis, C., J. Atmos. Sci., **60**, 2208 (2003).
- [56] Nicolis, C., J. Atmos. Sci., **61**, 1740 (2004).
- [57] Judd, K., C. Reynolds, T. Rosmond, and L. Smith, J. Atmos. Sci., **65**, 1749 (2008).
- [58] Nicolis, C., C. R. Perdigo and S. Vannitsem, J. Atmos. Sci., **66**, 766 (2009).
- [59] Ruelle, D., Publications mathematiques de l'IHES, **50**, 27 (1979).
- [60] Eckmann, J.-P., and D. Ruelle, Rev. Mod. Phys., **57**, 617 (1985).
- [61] Ruelle, D., *Chaotic Evolution and Strange Attractors*, Cambridge University Press (Cambridge, 1989).
- [62] Ott, E., *Chaos in dynamical systems*. Cambridge University Press (Cambridge, 1993).
- [63] Smith L., *Chaos: A very short introduction*, Oxford University Press (Oxford, UK, 2007).
- [64] Sprott, J. C., *Elegant Chaos*, World Scientific (Singapore, 2010).
- [65] Cencini M., F. Cecconi and A. Vulpiani, *Chaos. From simple models to complex systems*, World Scientific (Singapore, 2010).
- [66] Yoden, S., J. Meteorol. Soc. Jpn, **63**, 535 (1985).
- [67] Yano, J.-I, and H. Mukougawa, Geophys. and Astrophys. Fluid Dyn., **65**, 77 (1992).
- [68] Nese, J. M. and J. A. Dutton, J. Climate, **6**, 185 (1993).
- [69] Yoden, S., and M. Nomura, J. Atmos. Sci., **50**, 1531 (1993).
- [70] Nicolis, C., S. Vannitsem and J.-F. Royer, Q. J. R. Meteorol. Soc., **121**, 705 (1995).
- [71] Broer, H.W., Dijkstra, H.A., Simó, C., Sterk, A.E., and Vitolo, R., DCDS-B, **16**, 73 (2011).
- [72] Szunyogh, I., E. Kalnay and Z. Toth, Tellus, **49A**, 200 (1997).
- [73] Snyder, C. and T. Hamill, J. Atmos. Sci., **60**, 683 (2003).
- [74] Lucarini, V., A. Speranza and R. Vitolo, Physica D, **234**, 105 (2007).
- [75] Benzi, R., and G. F. Carnevale, J. Atmos. Sci., **46**, 3593 (1989).
- [76] Nicolis, C. and G. Nicolis, Phys. Rev., **43A**, 5720 (1991).
- [77] Nicolis, C., Q. J. R. Meteorol. Soc., **118**, 553 (1992).
- [78] Trevisan, A., J. Atmos. Sci., **50**, 1016 (1993).
- [79] Vannitsem, S. and C. Nicolis, J. Geophys. Sci., **99**, 10377 (1994).
- [80] Trevisan, A. and F. Pancotti, J. Atmos. Sci., **55**, 390 (1998).
- [81] Boffetta, G., P. Giuliani, G. Paladin, and A. Vulpiani, J. Atmos. Sci., **55**, 3409 (1998).
- [82] Yamane, S. and S. Yoden, J. Atmos. Sci., **58**, 1066 (2001).
- [83] Chu, P., L. Ivanov, T. Margolina and O. Melnichenko, J. Atmos. Sci., **59**, 2860 (2002).
- [84] Aurell, E., G. Boffetta, A. Crisanti, G. Paladin, and A. Vulpiani, Phys. Rev. Lett., **77**, 1263 (1996).
- [85] Bohr T., M. Jensen, G. Paladin, A. Vulpiani, *Dynamical systems approach to turbulence*, Cambridge University Press (Cambridge, UK, 1998).
- [86] Molteni F. and T. N. Palmer, Q. J. R. Meteorol. Soc., **119**, 269 (1993).
- [87] Buizza, R. and T. N. Palmer, J. Atmos. Sci., **52**, 1434 (1995).
- [88] Erhendorfer M. and R. M. Errico, J. Atmos. Sci., **52**, 3475 (1995).
- [89] Gelaro, R., C. A. Reynolds and R. M. Errico, Q. J. R. Meteorol. Soc., **128**, 205 (2002).
- [90] Ghil, M., and S. Childress, *Topics in Geophysical Fluid Dynamics: Atmospheric dynamics, dynamo theory and climate dynamics*, Springer-Verlag (New York, 1987).
- [91] Houghton, T., *The physics of the atmosphere*. Cambridge University Press (Cambridge, 1984).
- [92] Daley, R., *Atmospheric data assimilation*, Cambridge University Press, (Cambridge, 1991).
- [93] Vallis, G., *Atmospheric and Oceanic Fluid Dynamics*, Cambridge University Press (Cambridge, UK, 2006).
- [94] Hoskins, B.J., M. McIntyre, and W. Robertson, Q. J. R. Meteorol. Soc., **111**, 877 (1985).
- [95] Veronis, G., J. Atmos. Sci., **20**, 577 (1963).
- [96] Lorenz, E. N., Tellus, **17**, 321 (1965).
- [97] Charney, J. G. and J. G. DeVore, J. Atmos. Sci., **36**, 1205 (1979).
- [98] Charney, J. G. and D. M. Straus, J. Atmos. Sci., **37**, 1157 (1980).
- [99] Yao, M.S., J. Atmos. Sci., **37**, 29 (1980).
- [100] Reinhold, B. B. and Pierrehumbert, R. T., Mon. Weather Rev., **110**, 1105 (1982).
- [101] Lorenz E.N., J. Atmos. Sci. **41**, 1933 (1984).
- [102] Cehelsky P. and K.K. Tung, J. Atmos. Sci., **44**, 3282 (1987).
- [103] Vallis, G., J. Geophys. Res., **93**, 13979 (1988).
- [104] Maas L., Tellus, **46A**, 671 (1994).
- [105] Jiang, S., Jin, F.-F., and Ghil, M., J. Phys. Oceanogr., **25**, 764 (1995).
- [106] Yoden, S., Nonlin. Anal. Theor. Meth. Appl., **30**, 4607 (1997).
- [107] Van Veen, L., Dynam. Atmos. Oceans, **37**, 197 (2003).
- [108] Dijkstra, H. A. and Ghil, M., Rev. Geophys., **43**, RG3002 (2005).
- [109] Simonnet E., M. Ghil, H. Dijkstra, J. Marine Res, **63**, 931 (2005).
- [110] Pierini, S., J. Phys. Oceanogr., **41**, 1585 (2011).
- [111] Vannitsem, S., Clim. Dyn., **42**, 1981 (2014).
- [112] Vannitsem, S., and L. De Cruz, Geosci. Model Dev., **7**, 649 (2014).
- [113] De Cruz L., J. Demaeyer, and S. Vannitsem, Geosci. Model Dev., **9**, 2793 (2016).
- [114] Chen Z.-M., Int. J. Bifurcation Chaos, **26**, 1630020 (2016).
- [115] Vannitsem, S., Geophys. Res. Lett., **42**, 8615 (2015).
- [116] Vannitsem S., J. Demaeyer, L. de Cruz, and M. Ghil, Physica D, **309**, 71 (2015).
- [117] Marshall, J., and F. Molteni, J. Atmos. Sci., **50**, 1792 (1993).
- [118] Legras B. and R. Vautard, ECMWF Seminar Proceedings *Predictability, Volume I*, 143 (1995).
- [119] Kuptsov, P. V., U. Parlitz, J. Nonlin. Sci. **22**, 727762 (2012).
- [120] Vannitsem, S. and V. Lucarini, J. Phys. A, **49**, 224001 (2016).
- [121] Froyland, G., T. Hüls, G. P. Morriss, T. M. Watson, Physica D, **247**, 19 (2013).

- [122] Ginelli, F., P. Poggi, A. Turchi, H. Chaté, R. Livi, A. Politi, Phys. Rev. Lett., **99**, 130601 (2007).
- [123] Pazó, D., I. G. Szendro, J. M. López, and M. A. Rodríguez, Phys. Rev. E, **78**, 016209 (2008).
- [124] Gallez, D. and A. Babloyantz, Physics Letters, **161**, 247 (1991).
- [125] Abarbanel H.D.I, R. Brown and M.B. Kennel, J. Non-linear Science, **1**, 175 (1991).
- [126] Branstator, G., Mon. Wea. Rev., **114**, 2628 (1986).
- [127] Gallavotti, G., E. G D Cohen, J. Stat. Phys., **80**, 931 (1995).
- [128] Trevisan A and F. Uboldi, J. Atmos. Sci., **61**, 103 (2004).
- [129] Carrassi, A., A. Trevisan and F. Uboldi, Tellus A, , 101 (2007).
- [130] Nicolis C., G. Nicolis, and Q. Wang, Int. J. Bifurcation Chaos, **02**, 263 (1992).
- [131] Vannitsem S. and C. Nicolis, Int. J. Bifurcation Chaos, **6**, 2223 (1996).
- [132] Vallis, G., Q. J. R. Meteorol. Soc., **111**, 1039 (1985).
- [133] Wang, S., J. Math. Anal. Appl., **165**, 266 (1992).
- [134] Lions J. L., O.P. Manley, R. Temam, and S. Wang, J. Atmos. Sci., **54**, 1137 (1997).
- [135] Berner, J., G.J. Shutts, M. Leutbecher and T.N. Palmer J. Atmos. Sci., **60**, 2208 (2009).
- [136] Weisheimer A. , S. Corti, T.N. Palmer, F. Vitart, Phil. Trans. R. Soc., **A372**, 20130290 (2014).
- [137] Seki, K., V. Balakrishnan, and G. Nicolis, Phys. Rev. E., **47**, 155 (1993).
- [138] Chu, P.C. and L.M. Ivanov, Nonlin. Proc. Geophys., **12**, 1 (2005).
- [139] Vannitsem, S., Phil. Trans. R. Soc., **A372**, 20130282 (2014).
- [140] Ghil, M., Discr. Cont. Dyn. Systems, **37**, 189 (2017).
- [141] Philander, S. G. H., *El Niño, La Niña, and the Southern Oscillation*, Academic Press, San Diego, 293 pp (1990).
- [142] Smith, D. M., A.A. Scaife, R. Eade and J.R. Knight, Q.J.R. Meteorol. Soc., **142**, 611 (2016).
- [143] Kravtsov, S., W. K. Dewar, M. Ghil, J.C. McWilliams and P. Berloff, Physica D, 237, 584 (2008).
- [144] Brachet, S., F. Codron, Y. Feliks, M. Ghil, H. Le Treut and E. Simonnet, J. Clim., 25, 1847 (2012).